Volume 15, Issue 6, 152526 (1-28)

Journal of Nanostructure in Chemistry (JNSC)

https://doi.org/10.57647/jnsc.2025.1506.26

Green synthesis of Ag_2O/B@OP-CDs nanocomposite for pipette tip solid-phase extraction (PT-SPE) of mercury from food samples: optimization by artificial neural networks (ANN) and evolutionary polynomial regression (EPR)

Mahboube Shirani [1,*], Qamar Salamat [2], Mahtab Rezaei Payam [1], Mohammadjavad Jahanshahi [1], Mohammad Saleh Barghi Jahromi[3], Mahboobe Amirani Poor [4], Mustafa Soylak [2,5,6,7,*]

[1] *Department of Chemistry, Faculty of Science, University of Jiroft, Jiroft, P. O. Box 7867161167, Iran*
[2] *Department of Chemistry, Faculty of Sciences, Erciyes University, Kayseri, Turkey*
[3] *Department of Mechanical Engineering, University of Jiroft, Jiroft, Iran*
[4] *Central Laboratory, University of Jiroft, Jiroft, 7867161167, Iran*
[5] *Technology Research and Application Center (ERU-TAUM), Erciyes University, 38039 Kayseri, Turkey*
[6] *Turkish Academy of Sciences (TUBA), Çankaya, Ankara, Turkey*
[7] *Nano Bioanalytical Chemistry Center (NBACC), Khazar University, Mahsati Str 41, AZ-1096, Baku, Azerbaijan*

[*] **Corresponding authors:** m.shirani@ujiroft.ac.ir, msoylak@gmail.com, soylak@erciyes.edu.tr

Original Research

Received:
1 August 2025

Revised:
15 September 2025

Accepted:
28 September 2025

Published in Issue:
31 December 2025

Abstract

Mercury contamination in food remains a critical public health concern due to its extreme toxicity and bioaccumulation in the environment. Developing rapid, sensitive, and environmentally sustainable methods for its detection is of great importance. In this study, a biodegradable nanocomposite comprising silver oxide nanoparticles and boron-doped carbon quantum dots derived from orange peel waste was introduced. This material served as a high-performance sorbent for pipette-tip solid-phase extraction of inorganic mercury from food samples. Synthesized via a green hydrothermal process using agricultural waste, the resulting ternary nanohybrid leverages the synergistic affinity of Ag_2O and OP-CDs toward Hg (II), yielding exceptional extraction efficiency. Notable advantages included rapid extraction kinetics, minimal consumption of sorbent and solvent, and the elimination of toxic reagents, thereby fully aligning with the principles of green analytical chemistry. Extraction parameters were optimized using chemometric and statistical approaches, specifically artificial neural networks and evolutionary polynomial regression, to ensure robust performance. Under optimized conditions, the method represented trace-level detection capability and excellent precision in diverse food matrices. Comprehensive green metric evaluation confirms the sustainability of the approach. This sustainable, AI-enhanced extraction strategy provides an efficient and practical solution for trace mercury analysis in food, with broad potential in food safety monitoring.

Keywords: Carbon quantum dots; Green metrics evaluation; Inorganic mercury; Nanocomposite; Pipette tip solid phase extraction

Cite this article: Shirani, M., Salamat, Q., Rezaei Payam, M., Jahanshahi, M. J., Barghi Jahromi, M. S., Amirani Poor, M., Soylak, M. Green synthesis of Ag_2O/B@OP-CDs nanocomposite for pipette tip solid-phase extraction (PT-SPE) of mercury from food samples: optimization by artificial neural networks (ANN) and evolutionary polynomial regression (EPR). *J Nanostruct Chem* **15**(06), 152526 (2025).

1.Introduction

Concerning the environmental protection issues, food safety, and food chemistry rules, and also achieving healthy food with high purity, the determination of trace/ultra-trace levels of heavy metals is indispensable [1,2]. Mercury is regarded as one of the most toxic, mutagenic, and carcinogenic elements by the World Health Organization (WHO) [3]. Mercury exists in water, soil, air, and consequently in the food chain in different forms, including inorganic, elemental, or organometallic forms (Hg^{2+}, Hg^{0}, and methyl/ethyl mercury) [4,5]. The common exposure sources to mercury are dental amalgam, cosmetic substances, pharmaceuticals, and contaminated foods, particularly seafood [6,7]. Moreover, contaminated water and agricultural products are other sources of mercury pollution, which can transfer mercury to the human and animal food chain. Mercury can cause various neurodegenerative disorders, such as Alzheimer's, amyotrophic lateral sclerosis, Parkinson's, and its high dosages are deadly [8]. Therefore, the separation and determination of mercury in foodstuffs is crucial. Owing to the chronic poisoning effects of mercury, the Food and Agriculture Organization and the World Health Organization (FAO/WHO) have determined the maximum permissible intake limit of 5 μg kg^{-1} body weight per week [9]. Hence, the combination of a potent sample treatment technique and an extremely sensitive detection method is required to determine the amount of mercury in food samples. Liquid-liquid extraction [10,11], solid phase extraction (SPE) [12], solid phase microextraction (SPME) [13], and liquid phase microextraction (LPME) [5] are among the commonly used sample treatment techniques. In addition, dispersive liquid-liquid microextraction (DLLME) [14], and its variants such as SPE-DLLME [15] are also applied for the separation and preconcentration of Hg(II) from different matrices. According to the pros and cons of each technique, the scientists decide which one to use. Solid phase extraction as a widely utilized technique, is recognized for its notable characteristics such as straightforward operation, minimal use of organic solvents, versatility in employing various sorbents with distinct functional groups as the solid phase, ease of automation, and straightforward advancement of the method. The Pipette Tip Solid Phase Extraction (PT-SPE) method is a sample separation and enrichment technique specifically used for the analysis of chemical, pharmaceutical, and biological substances [16]. This method has gained significant popularity due to its simplicity, speed, and efficiency in removing impurities and enriching target compounds [17]. The PT-SPE method is applied in various fields, including drug analysis, toxins, food safety, and environmental monitoring. This technique is particularly used in research and diagnostic laboratories for the isolation and analysis of specific compounds [18]. Various sorbents have been used in pipette tip SPE. Quantum dots are semiconductor nanoparticles with very small dimensions (typically in the range of 2 to 10 nanometers) and unique electrical and optical properties [19]. These properties arise from quantum effects at the nanoscale. Quantum dots can be synthesized using various methods, including physical, chemical, and biological methods [20]. Using natural materials such as agricultural waste as precursors for synthesizing quantum dots can lead to reduced costs and increased environmental sustainability, and also biocompatibility [21]. Previous studies have shown that materials decorated with Ag_2O or silver nanoparticles provide strong Hg^{2+} binding through adsorption and even amalgamation (e.g., sodalite-Ag-NPs systems, Ag_2O-decorated UiO-66 MOFs) [22,23]. Likewise, boron-doped (and co-doped) carbon quantum dots have been demonstrated to possess enhanced surface reactivity and electron-deficient sites, which improve interaction with heavy metal ions such as mercury [24-27]. Combining both modifications in a single nanocomposite is thus expected to deliver a synergistic enhancement in selectivity, sensitivity, and robustness under complex food matrices, which is the motivation behind Ag_2O/B co-doping in orange peel-derived carbon dots (OP-CDs) in the present work. The significant features of Ag_2O/B-decorated orange peel carbon quantum dots nanocomposite, i.e., Ag_2O/B@OP-CDs nanocomposite, have a wide range of futuristic applications in several fields, including photocatalysis, metal ions detection, sensing, bioimaging, medical diagnosis, and drug delivery [28]. This study aims to develop and validate a green, high-performance PT-SPE method coupled with flow injection microwave plasma atomic emission spectrometry (FI-MP-AES) for mercury determination in food, including white rice, wheat flour, fish, and shrimp, utilizing Ag_2O/B@OP-CDs nanocomposite and advanced AI-based optimization, with a focus on analytical

performance, environmental sustainability, and real sample applicability. Unlike previous approaches that focus primarily on either sorbent development or optimization techniques, this work advances the field by integrating a sustainable nanocomposite synthesized from biomass waste with statistical chemometric optimization tools, specifically artificial neural networks (ANN) and evolutionary polynomial regression (EPR). This dual innovation enables highly sensitive mercury extraction while maintaining strong compliance with green analytical chemistry principles.

2. Experimental

2.1. Chemicals

Mercury (II) nitrate monohydrate (≥98.0%, Merck Co., Germany) was utilized to prepare a stock solution containing 100 mg L^{-1} of mercury (II) in deionized water. The standard solution of 10 mg L^{-1} was prepared by serial dilution with deionized water to generate working solutions and calibration standards. Sodium hydroxide (NaOH), nitric acid (HNO_3), hydrogen peroxide (H_2O_2, 30%), sodium nitrate ($NaNO_3$, ≥99.0%), and other metal nitrate salts (used for coexisting ion interference studies) were all purchased from Merck Co., Germany, with the highest analytical grade available.Silver(I) oxide (Ag_2O, ≥99.0%) and amorphous boron powder (B, 95–97%) were obtained from Sigma-Aldrich (St. Louis, MO, USA) and used without further purification. Fresh orange peels, collected from local sources, were washed, oven-dried at 60 °C, and ground into powder using a household blender. All aqueous solutions were prepared using deionized water (resistivity ≥18.2 MΩ.cm) obtained from a Milli-Q water purification system (Millipore, USA). A 60 mL Teflon-lined stainless steel autoclave (Berghof, Germany) was used for hydrothermal synthesis. For purification steps, a 0.22 µm syringe filter (Millipore, USA) was employed, and freeze-drying was carried out using a lyophilizer (Christ Alpha 1–2 LDplus, Germany). Certified reference material Dogfish liver DOLT-3 (National Research Council of Canada) was used to assess the accuracy of mercury quantification in biological matrices.

2.2. Instrumentation

Microwave plasma atomic emission spectrometry (Agilent Technologies model 4210 MP-AES, USA) was employed to analyze mercury. The MP-AES analysis conditions were tabulated in Table S1. The single-line flow injection system with a peristaltic pump was coupled with the MP-AES system. Microwave digestion (Anton Paar, model Multiwave 5000, Austria) was used for the digestion of real samples. The characterisation of the sorbent was conducted using Fourier transform infrared spectroscopy (FT-IR) with a Perkin-Elmer Range 400 FT-IR spectrometer (Waltham, MA, USA), as well as SEM-EDX and EDS with a Zeiss Gemini 500 field emission scanning electron microscope (Oberkochen, Germany).

2.3. Sample Preparation

White rice and wheat flour were procured from a local supermarket in Jiroft, Kerman Province, Iran. Fish, shrimp, and crab were collected from the Persian Gulf, Bandar Abbas, Hormozgan Province, Iran. For each sample type, 0.3 g of homogenized sample was accurately weighed and transferred into a microwave digestion test tube. For the certified reference material DOLT-3, as well as for fish and shrimp samples, 1 mL of concentrated HNO_3 solution and 7 mL of H_2O_2 were added to each tube. The digestion was performed according to the microwave digestion program recommended by the manufacturer. After completion of the digestion process and cooling to room temperature, each sample was diluted to a final volume of 50 mL with deionized water (resistivity ≥18.2 MΩ.cm) and used for subsequent analysis. For white rice and wheat flour, 0.3 g of each sample was weighed and transferred to a digestion test tube. Then, 1 mL of deionized water and 3 mL of concentrated HNO_3 solution were added to each sample. After the digestion process, the final solution was diluted to 50 mL with deionized water and used for the analytical process. All digested samples were filtered through a 0.22 µm syringe filter prior to analysis. Each sample preparation was performed in triplicate to ensure reproducibility. Blanks and spiked samples were prepared and processed in parallel to monitor potential contamination and to assess recovery and method accuracy.

2.4. Synthesis of the Procedure of Ag_2O/B@OP-CDs Nanocomposite

Ag_2O was chosen for its known strong affinity for mercury ions, which arises from Ag–Hg

interactions, including adsorption and possible redox/amalgamation behavior (e.g., Ag-nanoparticle/Ag_2O-doped sorbents in sodalite matrices and Ag_2O-decorated MOFs show excellent Hg^{2+} removal efficiency) [22,23]. Boron doping was selected to enhance the surface reactivity and electron-deficient sites in carbon quantum dots, improving adsorption strength and functional binding toward Hg^{2+} (as seen in B-, N-co-doped CDs). Inserted together, Ag_2O and boron co-doping are expected to act synergistically to yield high selectivity, sensitivity, and stability under complex food matrix conditions.

The Ag_2O/B@OP-CDs nanocomposite was synthesized via a modified green hydrothermal method using orange peel waste as the carbon source [29]. Fresh orange peels were thoroughly washed with deionized water to remove surface impurities, then cut into small pieces and oven-dried at 60 °C until completely dehydrated. The dried peels were ground into a fine powder using a household blender.

For the synthesis, 2.0 g of powdered orange peel, 0.5 g of Ag_2O, and 0.5 g of amorphous boron powder were dispersed in 50 mL of deionized water under constant stirring to achieve a homogeneous suspension. The resulting mixture was transferred into a 60 mL Teflon-lined stainless-steel autoclave and subjected to hydrothermal treatment at 90 °C for 2 hours. After natural cooling to room temperature, the dark brown solution was centrifuged at 4000 rpm for 20 minutes to remove larger carbon residues. The supernatant containing the Ag_2O/B@OP-CDs nanocomposite was further purified by a second centrifugation at 4000 rpm for 10 minutes. The resulting solution was filtered through a 0.22 µm syringe filter to remove any remaining particulates. The filtrate was then freeze-dried to obtain the Ag_2O/B@OP-CDs nanocomposite as a brown powder. The dried nanocomposite was stored in opaque containers to prevent light-induced degradation until further use. For the preparation of OP-CDs as a control, the same procedure was followed, omitting the addition of Ag_2O and boron powders.

2.5. pH of the Isoelectric Point

To determine the zero-point potential (pH_{PZE}) of the nanocomposite, the pH of 12 Falcon tubes, each containing 10 mL of sodium nitrate (0.1 mol L^{-1}) and 10 mg of sorbent, was adjusted within the range of 1-12. The tubes were then shaken for 24 hours at 150 rpm at a temperature of 25 °C. The initial and final pHs were analyzed, resulting in a pH_{PZE} value of 6.3 (Fig. S1).

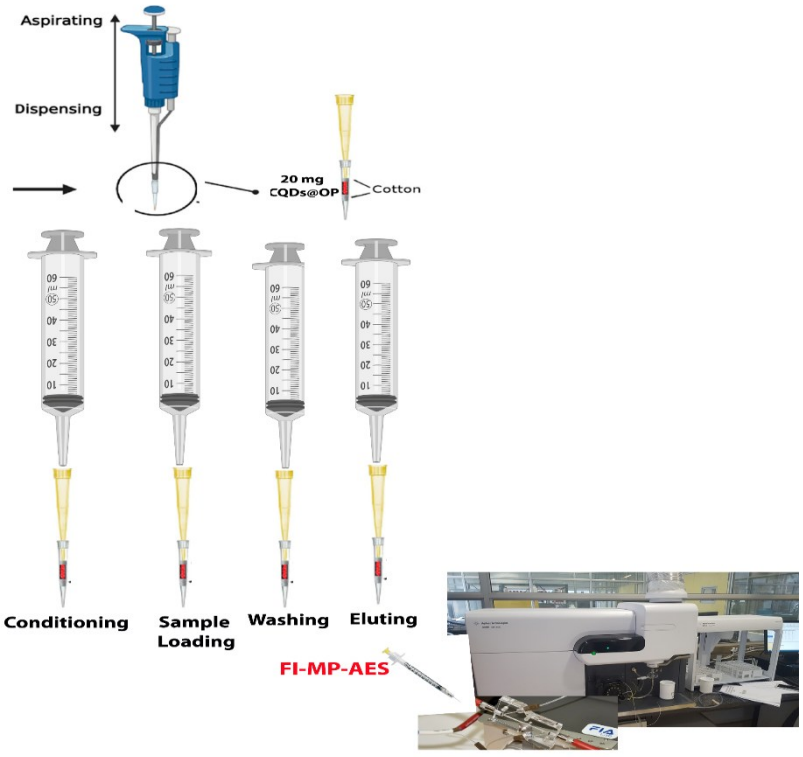

Schema 1. The schematic of the PT-SPE process

2.6. Analytical Procedure

A small piece of cotton was tightly packed at the end of a 200 µL pipette tip to serve as a support. Subsequently, 20 mg of Ag_2O/B@OP-CQDs nanocomposite was carefully introduced between two pieces of cotton within the pipette tip to ensure secure placement of the sorbent. A 1000 µL pipette tip was then fitted over the 200 µL tip, and the assembly was connected to a syringe, as illustrated in Scheme 1. Before sample loading, the sorbent was activated by passing deionized water through the pipette tip several times. The sample solution was then drawn through the homemade pipette tip assembly by aspirating with the syringe, allowing efficient adsorption of mercury ions onto the nanocomposite. For desorption, 100 µL of hydrochloric acid (2 mol L^{-1}) was aspirated to elute the bound mercury ions from the sorbent. The resulting 100 µL HCl solution containing Hg^{2+} was subsequently injected into the FI-MP-AES instrument for quantification.

2.7. Quantitative Calculation of the Proposed Process

According to the preliminary laboratory experiments, Ag_2O@B@OP-CDs-PT-SPE effectively preconcentrated Hg (II), after which the significant parameters were optimized using a univariable method. Furthermore, the enhancement factor (EF), extraction efficiency (EE) (%), and relative recovery (RR) (%) were computed as follows [29,30]:

1) $EF = \frac{C_{ES}}{C_{aq}}$

2) $EE\ (\%) = \frac{C_{ES}\,V_{ES}}{C_{aq}V_{aq}} \times 100$

3) $RR\ (\%) = \frac{C_{founded} - C_{Real}}{C_{added}} \times 100$

Where C_{ES} and V_{ES} the concentration and volume of the analyte in the elution solvent and C_{aq} and V_{aq} are the concentration and volume of the analyte in the aqueous phase.

2.8. Statistical Analysis

Statistical analysis was done using GraphPad Prism 8 software (USA). Data were presented as means ± standard deviation (SD).

Statistical differences of importance regarding the effects of solution pH, sorbent dosage (mg), vortex time (min), HCl concentration (mol L^{-1}), HCl volume (µL), desorption time(s), NaCl concentration (mol L^{-1}), and sample volume (mL) were assessed by a one-way analysis of variance (ANOVA), followed by Dunnett's multiple comparisons test, with a single pooled variance. Dunnett's test suggests comparisons were made against a specific control group. The lack of significance (ns) implies minimal deviation from this control across most groups. The labels (ns) suggest that, for certain conditions, no statistically significant differences in extraction efficiency were detected compared to the control group. Statistical significance was denoted by *($P < 0.05$), **($P < 0.01$), ***($P < 0.001$), and ****($P < 0.0001$).

2.8.1. *Artificial Neural Network (ANN) Method*

Scheme 2 shows the Artificial Neural Network (ANN) flowchart. The ANN, with ten layers including an input layer, uses randomly selected data. Input parameters are pH, desorption time, HCl concentration/volume, ionic strength, sample volume, sorbent, and vortex time. Random data selection ensures comprehensive ANN training to model relationships between inputs and experimental outcomes, as shown in Scheme 2. These parameters are crucial for accurate ANN performance. In this investigation, a multilayer perceptron (MLP) neural network, implemented within the MATLAB software environment (version 2018), served as the primary modeling tool. This specific type of artificial neural network architecture is characterized by a layered structure, commencing with an input layer responsible for receiving the initial data. Subsequently, the network incorporates one or more hidden layers, each comprising interconnected neurons that perform complex transformations on the input data. The processed information then propagates to the final layer, known as the output layer, which generates the ultimate prediction or result. The configuration of the MLP network employed in this study aligns with established methodologies, as evidenced by prior research endeavors that have successfully utilized similar neural algorithms in the context of kinetic studies [31,32]. To determine the optimal number of neurons within the hidden layer(s), an iterative, empirical approach was adopted, involving a process of trial and error. Specifically,

approximately 50 independent training runs were conducted, each with a different network configuration, to identify the most effective structure.

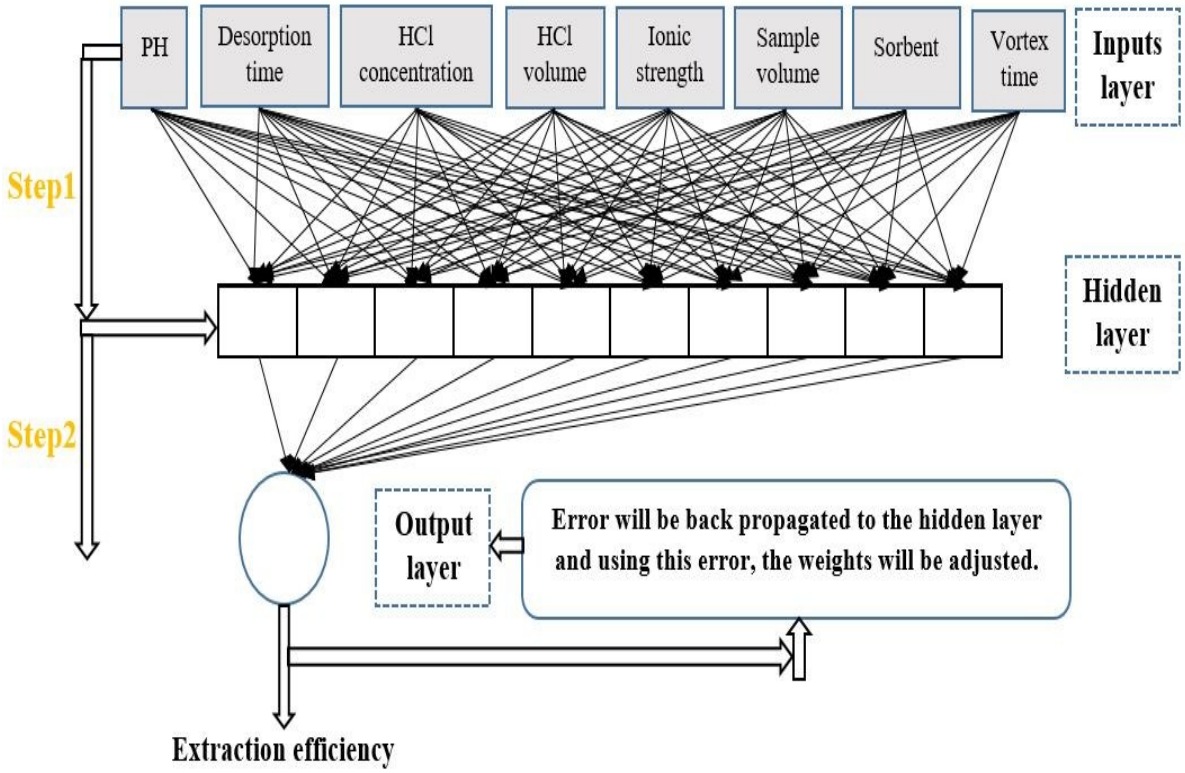

Scheme 2. ANN structure considered in this research

The selection of the best structure was based on a comprehensive evaluation of the output data generated by each run, in conjunction with an assessment of the relative error associated with the predictions. A visual representation of the ANN model structure, illustrating the relationships between input conditions, output predictions (specifically, extraction efficiency), and the network's internal architecture, is provided in Scheme 2. A linear activation function was used for the input layer to directly pass data through, while a tangent sigmoid function was used for the output layer to constrain predictions between -1 and 1, which is useful for many prediction tasks. The training phase employed a scaled conjugate gradient algorithm to efficiently optimize the network parameters and minimize prediction error. The normalized dataset was split into training (70%), validation (15%), and testing (15%) subsets. The normalized dataset was split into training (70%), validation (15%), and testing (15%) subsets. The training set allowed the model to learn patterns, the validation set fine-tuned hyperparameters to prevent overfitting, and the testing set assessed the model's generalization performance on unseen data. The best-performing model was selected based on minimizing Root Mean Squared Error (RMSE) and Coefficient of Variation (COV), and maximizing R-squared (R^2), ensuring both minimal prediction error and high statistical accuracy [33,34].

4) $$RMSE = \sqrt{\frac{1}{N}\sum_{i=1}^{N}\left(x_A - x_p\right)^2}$$

5) $$COV = \frac{RMSE}{\frac{1}{N}\sum_{i=1}^{N} x_p^2}$$

6) $$R^2 = 1 - \frac{\sum_{i=1}^{N}\left(x_A - x_p\right)^2}{\sum_{i=1}^{N} x_p^2}$$

2.8.2. *Evolutionary Polynomial Regression (EPR) Method*

Grey-box models, such as EPR, are conceptual models that bridge white-box and black-box approaches. Developing these models involves simplifying underlying processes to derive mathematical equations that capture essential system behavior. Parameter prediction, a key step,

involves calculating input and output data within a defined parameter range, as detailed by Giustoolisi and Savic (2006). EPR often uses polynomial equations to represent relationships between input and output variables. However, limited information exists on EPR's application to complex system performance prediction, warranting further research. EPR has been applied in various fields, including hydroinformatics and environmental challenges, demonstrating its adaptability to complex problems [35]. For instance, it has been used to optimize solar drying systems for medicinal plants, showcasing its potential in agricultural and environmental engineering, particularly in renewable energy applications. EPR employs a two-stage analytical approach. First, a genetic algorithm (GA) identifies optimal model structures by exploring potential configurations. Second, linear regression quantifies model parameters using least squares optimization to ensure accurate data fitting. These steps generate a comprehensive mathematical equation representing the EPR model, providing a tool for prediction and analysis [36]. This model predicts y based on input data X, adjustable parameters aj, and a function F(X). An optional bias, ao, can be included for increased accuracy. EPR builds equations to define the relationships between X, aj, F(X), and ao (if included), and y by strategically selecting contributing factors. This allows for a flexible representation of the system's behavior.

2.8.3. *Genetic Algorithm (GA) Method*

GA offers a robust optimization approach, providing a means to efficiently search complex solution spaces. The performance of optimization processes that leverage GAs is a crucial consideration. Evaluating this performance involves analyzing factors such as convergence rate, solution quality, and computational cost. A well-tuned GA can effectively identify near-optimal solutions within a reasonable timeframe, while a poorly configured algorithm may struggle to converge or produce unsatisfactory results. Therefore, understanding and optimizing the performance characteristics of GAs is essential for successful application in various domains [37]. GA optimizes models by finding the input parameters that maximize output. Because GAs are minimization algorithms, the objective function is defined as the negative of the model's output, converting the maximization problem into a minimization problem. This allows GAs to efficiently identify the optimal solution that maximizes the model's original output. In other studies, on the adsorption of crystal violet on magnetic activated carbon, GAs have been used [38].

3. Results and Discussion

3.1. Characterization

The synthesized Ag_2O/B@OP-CDs nanocomposite was systematically characterized using Fourier-transform infrared spectroscopy (FTIR), X-ray diffraction (XRD), Field emission scanning electron microscope (FE-SEM), and Scanning electron microscopy with energy dispersive X-ray spectroscopy (SEM-EDX) to assess their structural, morphological, and elemental properties.

3.1.1. *FTIR Spectroscopy*

FTIR analysis was conducted to ascertain the functional groups in the synthesized Ag_2O@B@OP-CDs nanocomposite (Fig. 1A). An intense absorption band about 3700 cm^{-1} signifies free O–H stretching, suggesting the presence of non-hydrogen-bonded hydroxyl groups or solitary surface hydroxyls. A large band about 3400 cm^{-1} is ascribed to hydrogen-bonded O–H stretching, indicating the presence of surface hydroxyl groups and adsorbed moisture. Two notable peaks identified at around 2970 cm^{-1} and 2900 cm^{-1} are attributed to the asymmetric and symmetric stretching vibrations of aliphatic C–H bonds, respectively. These are indicative of $–CH_2$ and $–CH_3$ groups found in the organic framework of biomass-derived carbon dots.

Oxidative carbonization of orange peel yields carbonyl groups, such as aldehydes or carboxylic acids, evidenced by an absorption band about 1720 cm^{-1}. The successful doping of boron is validated by a significant peak observed between 1450 and 1380 cm^{-1}, indicating B-O stretching. The C-OH bond deformation is indicated by the band at roughly 1260 cm^{-1}. The distinct signals observed between 1100 and 1000 cm^{-1}, which imply C-O-C and C-OH stretching, respectively, indicate the existence of alcohols, ethers, or esters. The presence of Ag_2O in the nanocomposite is corroborated by the detection of a band within the range of roughly 520 to 500 cm^{-1}, signifying the Ag-O stretching vibration. The production of a multifunctional hybrid nanomaterial

is validated by the identification and augmentation of functional groups in the Ag_2O/B@OP-CDs spectrum, relative to the individual precursors [39].

3.1.2. *X-ray Diffraction (XRD)*

The XRD pattern of the synthesized Ag_2O/B@OP-CDs nanocomposite (Fig. 1B) displays several distinct features that confirm the successful integration of its constituent components. A diffraction peak centred at approximately $2\theta = 21.5°$ is observed in both the OP-CDs and composite patterns, indicating the (002) plane of amorphous or turbostratic carbon. This feature signifies short-range graphitic ordering, typically found in carbon quantum dots (CDs) generated via low-temperature hydrothermal carbonization of biomass. The absence of prominent peaks in this region signifies that the carbon phase lacks long-range crystallinity. The shift from the standard graphite (002) peak at 26.6° indicates an augmentation in interlayer separation, typically linked to the existence of oxygen-containing surface functional groups.

The effective incorporation of Ag_2O nanoparticles is confirmed by the notable peaks in the composite pattern at approximately 2θ = 32.8°, 38.1°, 65.4°, and 82.3°, aligning with the (111), (200), (220), and (311) planes of cubic Ag_2O (JCPDS No. 41-1104). The presence of these peaks in the pure AgO spectrum further supports the notion that the crystalline structure of AgO remains unchanged after hydrothermal synthesis.

Moreover, multiple weaker and broader diffraction signals from the boron precursor remain evident in both the B and composite spectra, indicating the presence of amorphous or low-crystallinity boron-containing species. The composite spectrum presents a cohesive representation of the three components—CDs, B, and Ag_2O—confirming successful hybridization while maintaining the individual structural identities with minimal loss [40-42].

It should be noted that FTIR and XRD data were normalized before plotting to ensure comparability of spectral features. Consequently, the y-axis is displayed as normalized transmittance/intensity.

3.1.3. *SEM Analysis*

The surface morphology of the produced materials underwent a thorough analysis utilizing FE-SEM (Fig. 2). The micrographs of Ag_2O shown in Fig. 2(a–b) display polycrystalline aggregates identified by an uneven and coarse surface morphology, demonstrating the existence of chemically precipitated silver oxide particles. The observed agglomerates indicate crystalline formation lacking a defined morphology, consistent with low-temperature synthesis methods. The boron sample demonstrated in Fig. 2(c–d) has a flaky, sheet-like morphology marked by a highly wrinkled surface and layered texture, suggesting an amorphous or low-crystallinity structure. This morphology is advantageous for doping or surface modification applications because of its elevated surface roughness and reactivity. The OP-CDs images in Fig. 2(e–f) exhibit uniform, spherical morphology, with sizes ranging from approximately 100 to 500 nm. The particles exhibit smooth surface textures and minimal aggregation, suggesting efficient nucleation during the hydrothermal carbonization of orange peel biomass. Their uniformly distributed, spherical morphology is indicative of biomass-derived CDs and improves their solubility and surface functionalization potential. The final Ag_2O/B@OP-CDs nanocomposite shown in Fig. 2(g–h) displays irregular, porous aggregates composed of interconnected nanoscale domains. The sponge-like structure demonstrates the successful integration of Ag_2O and boron within the CD framework. The increased surface area and heterogeneity enhance the composite's effectiveness as an adsorbent for Hg (II) ions, providing multiple active sites for mercury binding via surface complexation and electrostatic interactions. The freeze-drying procedure preserved the porosity structure, thereby minimizing collapse or sintering of the composite particles [43].

3.1.4. *EDX Analysis*

The elemental analysis of the individual components and the final nanocomposite was performed using SEM–EDX, as shown in Fig. 2 (i–m). The spectrum of Ag_2O (i) confirms the presence of silver (Ag) and oxygen (O), showing weight percentages of 88.4% for Ag and 11.6% for O. The significant Ag peaks demonstrate the elevated purity and crystallinity of the synthesized silver oxide. The EDX spectrum of boron suggests a high concentration of elemental boron with some surface oxidation, as it shows a dominant B signal (95.02 wt%, 97.02 at%) with minor contributions from carbon and oxygen. The major elements detected in OP-CDs (k) were carbon

and oxygen, with weight percentages of 69.72% and 30.28%, producing atomic percentages of 75.41% and 24.59%, respectively. The results affirm the oxygen-rich characteristics of the carbon quantum dots, aligning with the FTIR findings and indicating the presence of oxygen-containing functional groups such as carboxyl, hydroxyl, and carbonyl. The functionalities improve the hydrophilicity, colloidal stability, and binding affinity of CDs for metal ions, including Hg(II). The final Ag_2O/B@OP-CDs nanocomposite (m) was examined via EDX, confirming the presence of all requisite elements: boron (74.24 wt%, 84.14 at%), carbon (10.4 wt%, 10.75 at%), silver (11.55 wt%, 1.19 at%), and oxygen (3.81 wt%, 2.63 at%). This analysis illustrates the effective integration of Ag_2O and boron into the OP-CDs matrix. The identification of Ag and B peaks with carbon and oxygen confirms the ternary hybrid nature of the composite. This composition amplifies synergistic effects in metal ion adsorption, particularly for Hg (II), due to the collective contributions of silver oxide's affinity, boron doping, and CD surface functions [44].

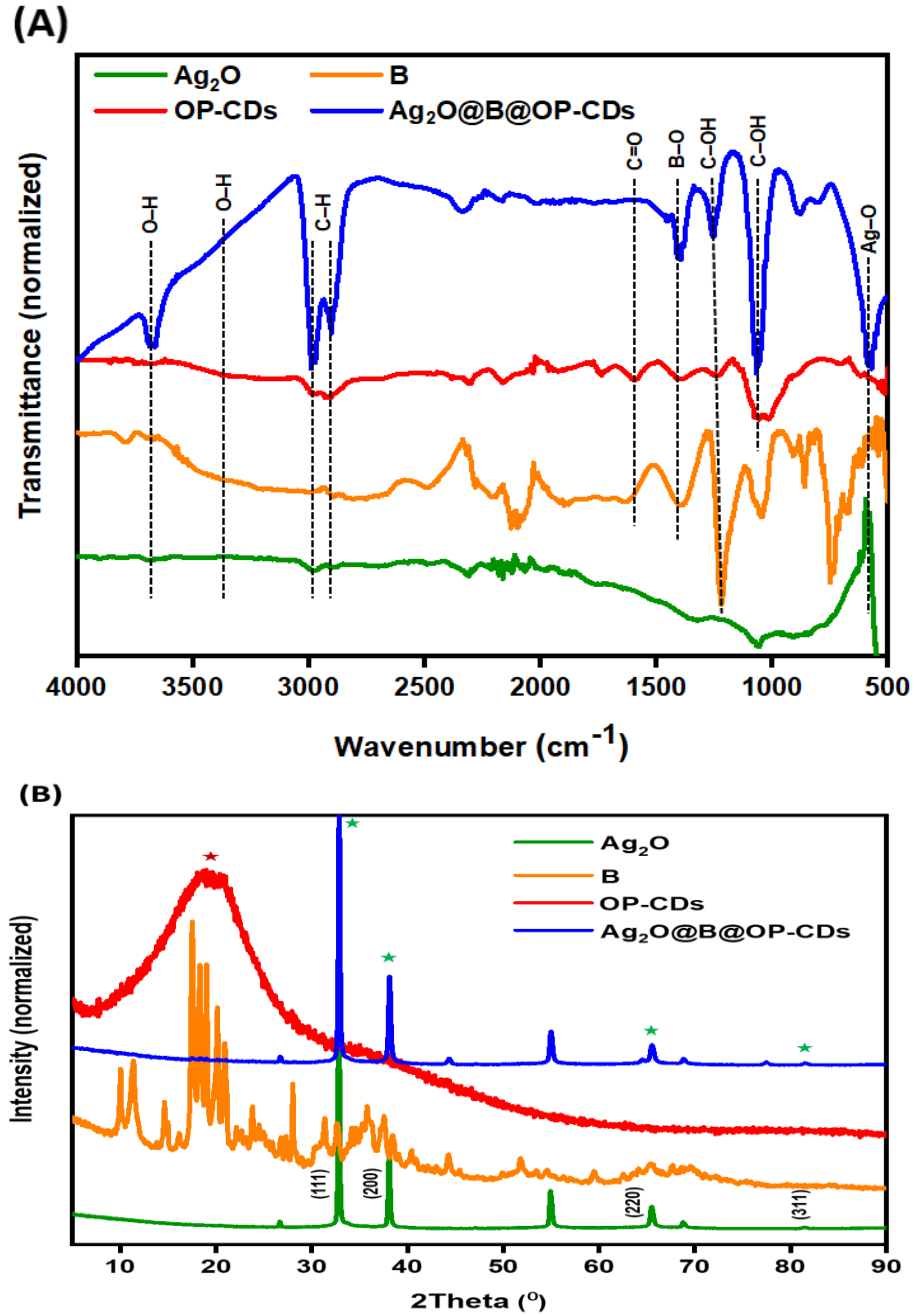

Figure 1. FTIR spectra **(A)** and XRD patterns **(B)** of polycrystalline clusters of Ag_2O, flaky Boron, spherical OP-CDs, and porous aggregates of Ag_2O/B@OP-CDs nanocomposites. Spectra are presented as normalized values to allow direct comparison across samples

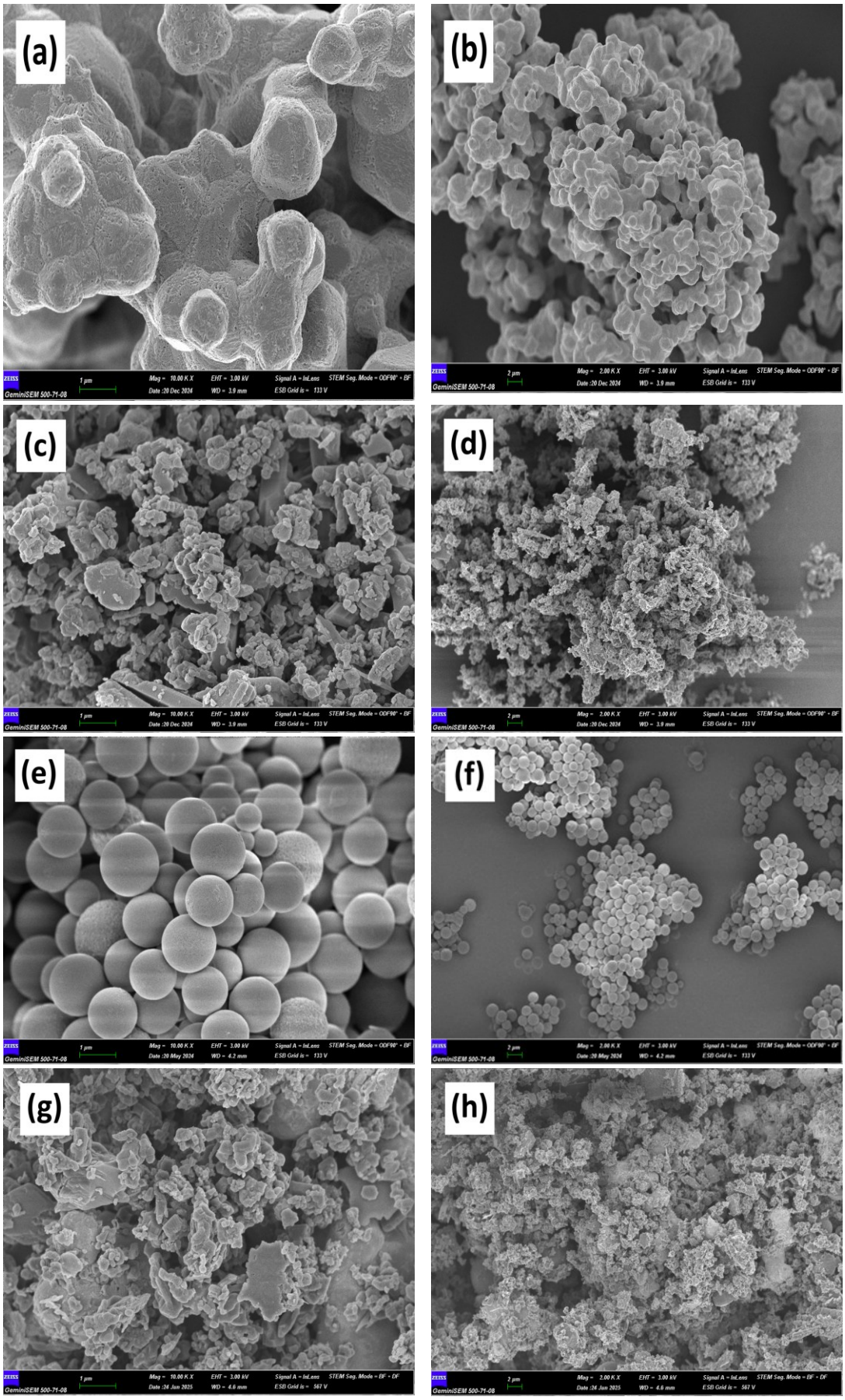
(a)
(b)
(c)
(d)
(e)
(f)
(g)
(h)

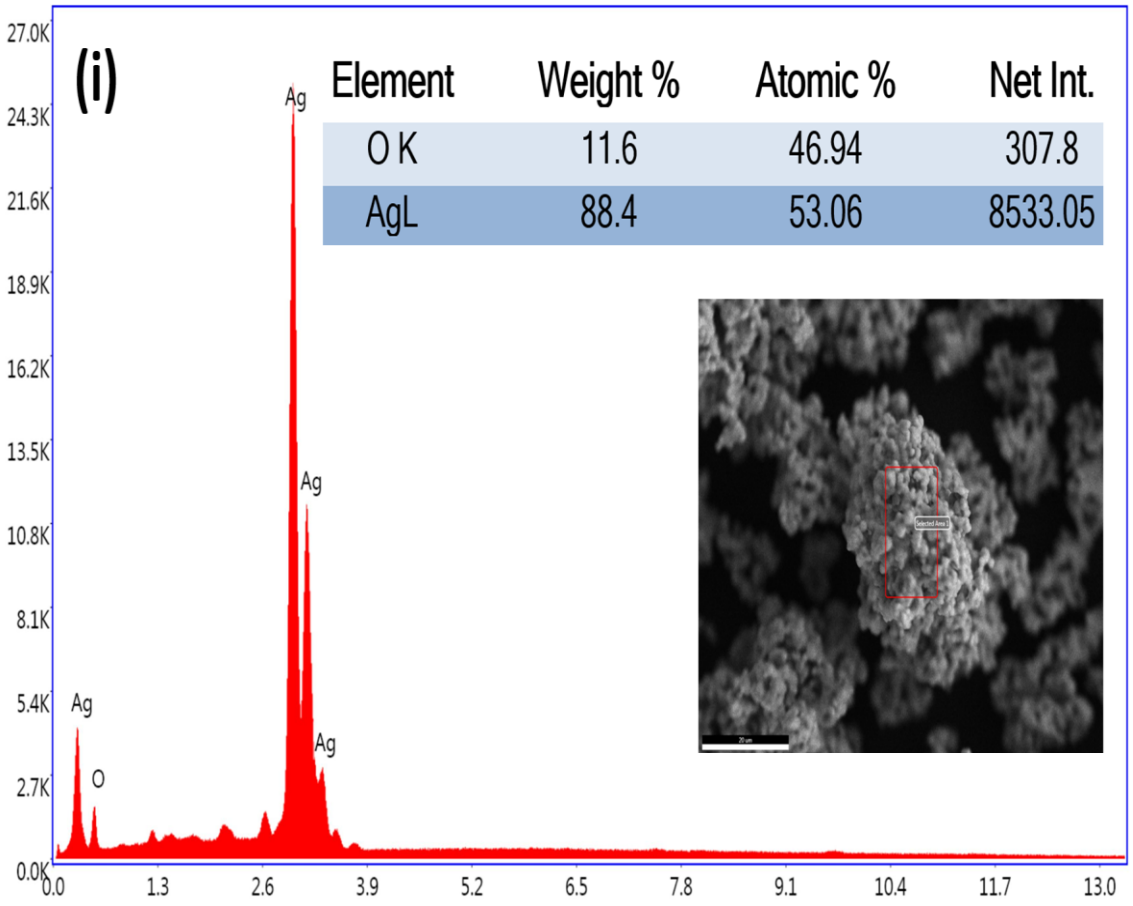
(i)
Element Weight % Atomic % Net Int.
O K 11.6 46.94 307.8
AgL 88.4 53.06 8533.05
Ag
Ag
Ag
Ag
O
27.0K
24.3K
21.6K
18.9K
16.2K
13.5K
10.8K
8.1K
5.4K
2.7K
0.0K
0.0 1.3 2.6 3.9 5.2 6.5 7.8 9.1 10.4 11.7 13.0

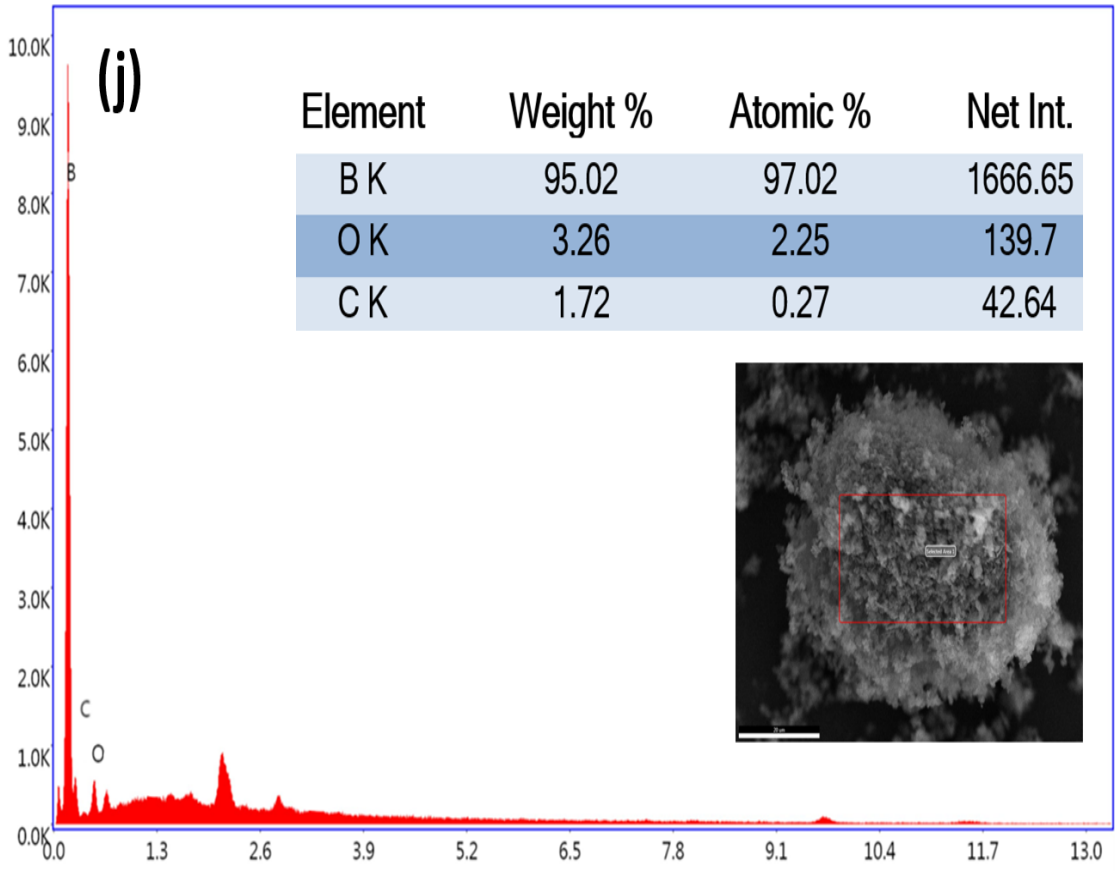
(j)
Element Weight % Atomic % Net Int.
B K 95.02 97.02 1666.65
O K 3.26 2.25 139.7
C K 1.72 0.27 42.64
B
C
O
10.0K
9.0K
8.0K
7.0K
6.0K
5.0K
4.0K
3.0K
2.0K
1.0K
0.0K
0.0 1.3 2.6 3.9 5.2 6.5 7.8 9.1 10.4 11.7 13.0

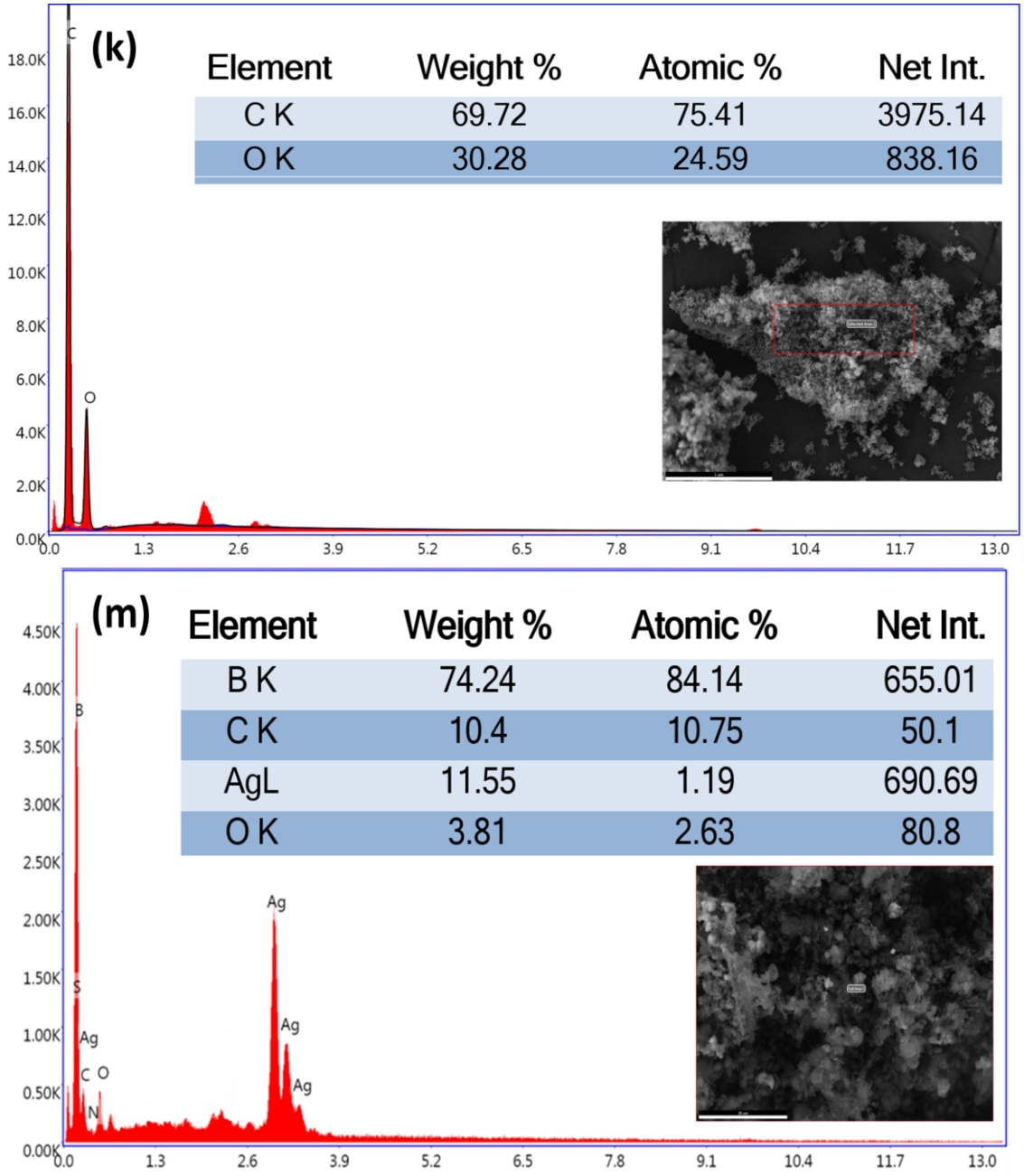

Figure 2. FE-SEM images of polycrystalline clusters of Ag_2O **(a & b)**, flaky Boron **(c & d)**, spherical OP-CDs **(e & f)**, and porous aggregates of Ag_2O/B@OP-CDs nanocomposites **(g & h)**. SEM-EDX spectra and the elemental composition of Ag_2O **(i)**, Boron **(j)**, OP-CDs **(k)**, and Ag_2O/B@OP-CDs nanocomposites **(m)**

3.2. The Study of Influential Parameters in Ag_2O/B@OP-CDs-PT-SPE of the Hg (II) Process

The influence of solution acidity or basicity on the functional groups of the extraction phase and analytes necessitates the examination of pH fluctuation in any analytical procedure. The impact of pH within the range of 3.5-10.5 was investigated, revealing that the extraction efficiencies rose from 3.5 to 6.5, reached maximum levels between 6.5 and 8.5, and then declined. At a pH of 6.3, the surface of Ag_2O/B@OP-CDs nanocomposites has a positive charge, repelling Hg^{2+} cations. Conversely, at pH levels exceeding 6.3, the surface becomes negatively charged, allowing for the adsorption of Hg^{2+} ions through electrostatic and Lewis acid-base interactions. The recoveries were quantitative and up to 96.0 %. Moreover, for pHs over 8.5, the hydrolysis of mercury ions occurs, and Hg^{2+} interacts with hydroxide groups and forms $Hg(OH)_2$ in the solution [45], and the extraction efficiency decreases. Hence, the optimum pH of 7.5 was selected for further studies.

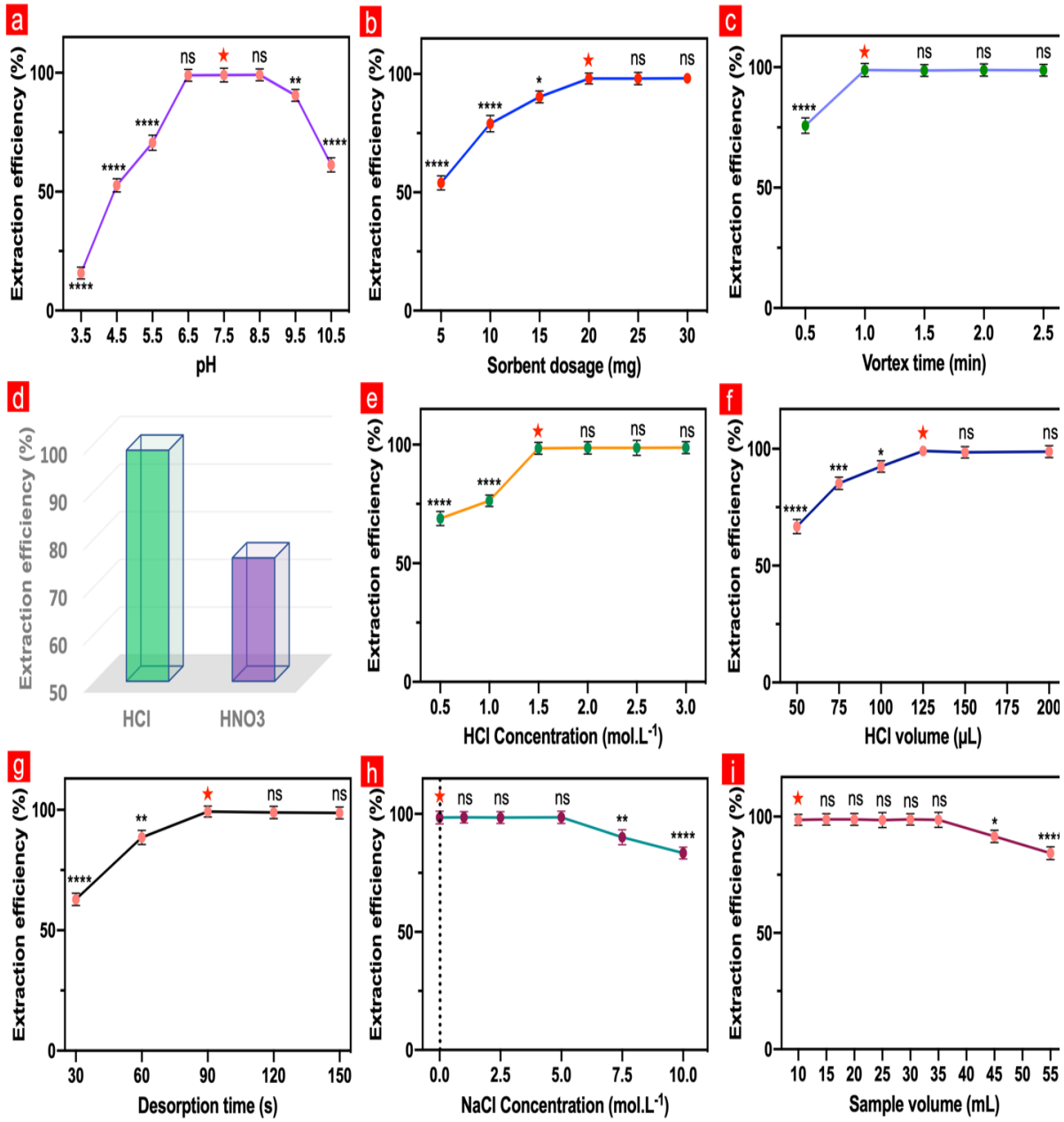

Figure 3 (a) solution pH, (b) sorbent dosage (mg), (c) vortex time (min), (d) desorption solvent type, (e) HCl concentration (mol L^{-1}), (f) HCl volume (µL), (g) desorption time (s), (h) NaCl concentration (mol L^{-1}), and (i) sample volume (mL) Data are expressed as mean ± SD based on three independent experiments and significant differences between groups appeared with (ns= not significant), *(P <0.05), **(P <0.01), ***(P <0.001), and ****(P <0.0001) using two-way ANOVA with Dunnett's multiple comparisons test, with individual variances computed for each comparison

The quantity of sorbent as the solid phase offers unoccupied active sites for the analyte to adhere to the sorbent's surface and interact with its functional groups. The quantity of sorbent, ranging from 5 to 50 mg, was examined, and as illustrated in Fig. 3 (b), the extraction efficiency improved from 5 to 20 mg and then stabilized. It shows that the amount of 20 mg sorbent is sufficient for the adsorption of mercury ions in the solution, and the active sites of 20 mg of Ag_2O/B@OP-CDs nanocomposites are enough to achieve the extraction efficiencies of about 99.0%. Consequently, an optimal quantity of 20 mg was placed in the pipette tip for further experiments. Desorption conditions, i.e., desorption solvent type and volume in solid phase extraction techniques, play an important role in the method's sufficiency.

The desorption solvent should interact strongly with the analyte to elute it from the sorbent. To this purpose, the effect of HNO_3 and HCl as desorption solvents was investigated, and as presented in Fig. 3 (c), HCl showed the best desorption efficiency and

could elute mercury ions with higher efficiency from the Ag_2O@B@OP-CDs.

The impact of HCl concentrations ranging from 0.5 to 2.5 mol L^{-1} was examined to elute the sorbent for the desorption of Hg (II) from its surface. The results indicate that 1.5 mol L^{-1} HCl exhibited the maximum extraction efficiency (Fig. 3 (d)). Moreover, the elution solvent volume was studied in the range 50-200 µL.

As shown in Fig. S1, the extraction efficiency was maximum for the volumes up to 125 µL, and it was chosen as the optimum.The ionic strength of the solution is characterized by the presence or absence of salts, primarily sodium chloride, which influences the salting-in or salting-out effects. Therefore, the concentrations of NaCl in the range of 0–10% (w/v) were added to the sample solution. As shown in Fig. 3 (e), the extraction efficiency is almost constant from 0-5 and then increases for the concentrations above 5 %.

At high concentrations, the viscosity of the solution increases, and the analyte transfer and interaction on the surface of the sorbent will be decreased. The analyte sample volume influences the preconcentration factor and extraction efficiency of the analytical process. The sample volume ranging from 10 to 60 mL was examined, and as illustrated in Fig. 3 (f), the extraction efficiency (%) remains steady and quantitative between 10 and 35 mL, subsequently declining. The volume of 35 mL was selected as optimum.

3.3. The Effect of Co-Existing Ions

The effect of some common coexisting ions, considered interfering ions, on the separation and preconcentration of Hg^{2+} through Ag_2O/B@OP-CDs-PT-SPE was studied. A solution of Hg^{2+} (50 µg L^{-1}) containing coexisting ions was prepared, and Ag_2O@B@OP-CDs- PT-SPE was performed. The amounts of interfering ions were determined according to the metal-to-interferent ratios (w/w) of 1:2000 for NH_4^+, K^+, Na^+, Ca^{2+}, Mg^{2+}, Al^{3+}, 1:250 for Ni^{2+}, Co^{2+}, $Fe^{3+,}$ and Cr^{3+}, Ag^+, 1:100 for Cu^{2+}, $Zn^{2+,}$ and Cu^{2+}, respectively. Recoveries of 95.1–99.6% were achieved for Hg^{2+} in the presence of interfering ions. The tolerance limits of the studied ions are tabulated in Table 1.The high recoveries obtained in the presence of large excesses of common cations demonstrate that the Ag_2O/B@OP-CDs nanocomposite is resistant to matrix-induced interferences. This tolerance indicates that mercury binding is highly specific and not significantly suppressed by competition from other ions, which is particularly important in complex food samples where multi-elemental backgrounds are unavoidable. The multi-functional surface chemistry of the nanocomposite, combining Ag-O active sites, boron-related moieties, and oxygenated groups from carbon quantum dots, likely contributes to this selectivity. These results further highlight the robustness of the proposed method compared to conventional sorbents that often suffer from strong matrix effects.

Table 1. Effect of coexisting ions on the percent recovery of Hg^{+2}

Interference	Interference to metal ion ratio	Recovery (%)
Na^+	2000	98.8±2.5*
K^+	2000	99.3±1.6
Mg^{2+}	2000	99.5±2.0
Ca^{2+}	2000	98.7±2.1
Al^{3+}	2000	99.0±2.0
Ni^{2+}	250	95.1±3.1
Cr^{3+}	250	96.6±2.4
Fe^{3+}	250	95.7±3.2
Co^{2+}	250	98.0±2.2
Cu^{2+}	100	97.3±2.6
Zn^{2+}	100	98.1±2.2
Cd^{2+}	100	99.4±2.5
NH_4^+	2000	99.6±2.0

* The data are for three replicates, and the results are expressed as recovery (%) ±standard deviation

3.4. Analytical Greenness Evaluation

3.4.1. *AGREE—Analytical Greenness Metric Approach*

To evaluate the greenness of analytical methods, some green metric tools have been introduced in recent years [24]. Three colors of red, yellow, and green with various definitions are used to show Analytical Greenness Metric Approach (AGREE) results with scores of 0-1, which are based on green chemistry aspects. The AGREE tool score for Ag_2O@B@OP-CDs-PT-SPE was 0.69. The prevalence of green in the final results, illustrated in Fig. 4 (a), confirms the reduced ecological impact and greener profile of the suggested method [46-48].

3.4.2. *AGREEprep—Analytical Greenness Metric for Sample Preparation*

The Analytical Greenness Metric for Sample Preparation (AGREEprep) tool is a green metric to consider the greenness of the sample preparation process, in which the final results are revealed according to ten classes, with the sub-scores of 0 to 1, containing some colorful sections. Each color represents a certain environmental concept [49].

3.4.3. *Blue Applicability Grade Index (BAGI)*

Blue Applicability Grade Index (BAGI) offers another approach to judge the practicality and efficiency of the method [50]. Its concept is aimed at efficiency and realistic applicability in practice; the methods should be judged regarding, for instance, factors like throughput, automation, or the amount of sample needed. Each criterion is graded from 1 to 10, and its geometric mean results in the BAGI score. Its balanced nature does not allow any factor to bias the assessment towards a specific outcome; hence, the grade will be fully representative. A BAGI score signifies that it is an extremely useful and efficient technique for optimizing time and cost consumption by reducing risks, thus giving effective results. Though it does not involve sustainability or environmental safeguards, this score confirms the suitability of the method for practical and realistic applications factor that shows its value to both the researchers and the practitioners [48]. According to the pictogram represented in Fig. 4 (c), the blueness score of the methodology is 62.5 %, which means the method is recommendably and acceptably green. Taken together, the AGREE, AGREEprep, and BAGI results not only confirm the environmental credentials of the proposed method but also demonstrate tangible sustainability advantages compared with conventional extraction approaches. The reliance on agricultural waste (orange peels) as a precursor reduces raw material costs and valorizes biomass that would otherwise contribute to environmental burden. The elimination of toxic organic solvents and reduction of sample and sorbent quantities minimize chemical waste and energy-intensive disposal requirements, aligning with EU and global sustainability policies for green laboratories. In addition, the favorable BAGI score highlights the method's operational advantages: lower cost, faster throughput, and reduced occupational risks, making it highly suitable for real-world food safety and environmental monitoring laboratories, where practicality and sustainability are equally critical.

3.4.5. *The Carbon Footprint Reduction Index (CaFRI)*

The Carbon Footprint Reduction Index (CaFRI) is another tool for the enhancement and assessment of analytical methods' sustainability, which focuses on the greenhouse gas emissions [51]. Moreover, CaFRI focuses on the energy-conserving protocols. CaFRI overcomes other greenness tools by presenting a standardized approach for the consideration of carbon footprint reduction strategies. It assigns a numerical rating based on direct CO_2 emission factors such as energy efficiency and indirect factors like sample storage, transportation, waste management, and reagent use.

3.5. Data Results using ANN

In this work, two artificial neural network methods, namely ANN and EPR, are used to model and predict the extraction efficiency based on different input parameters. Fig. 5 (a to h) and Fig. 6 (a1 to h1) display scatter plots comparing experimental extraction efficiency (Exp) with predicted extraction efficiency from ANN and EPR models, respectively. Fig. 5 (a) to (h) shows the R^2 values for the considered parameters in the range of 0.997 to 1, indicating a strong linear correlation and excellent predictive ability of the ANN model to predict the experimental data. As shown in Fig. 5 (e), for ionic

strength, $R^2 = 1$ is shown with $y = 0.9992x + 0.0692$, indicating a perfect fit of the ANN model, which is very important. In other studies, the optimal values of R^2=0.996 have been obtained for the Efficient removal of crystal violet [33]. In another study, using the ANN algorithm to remove crystal violet by zinc oxide nanorods loaded on activated carbon, the value of R^2=0.992 was obtained [52]. This indicates the appropriate prediction of the ANN artificial network.

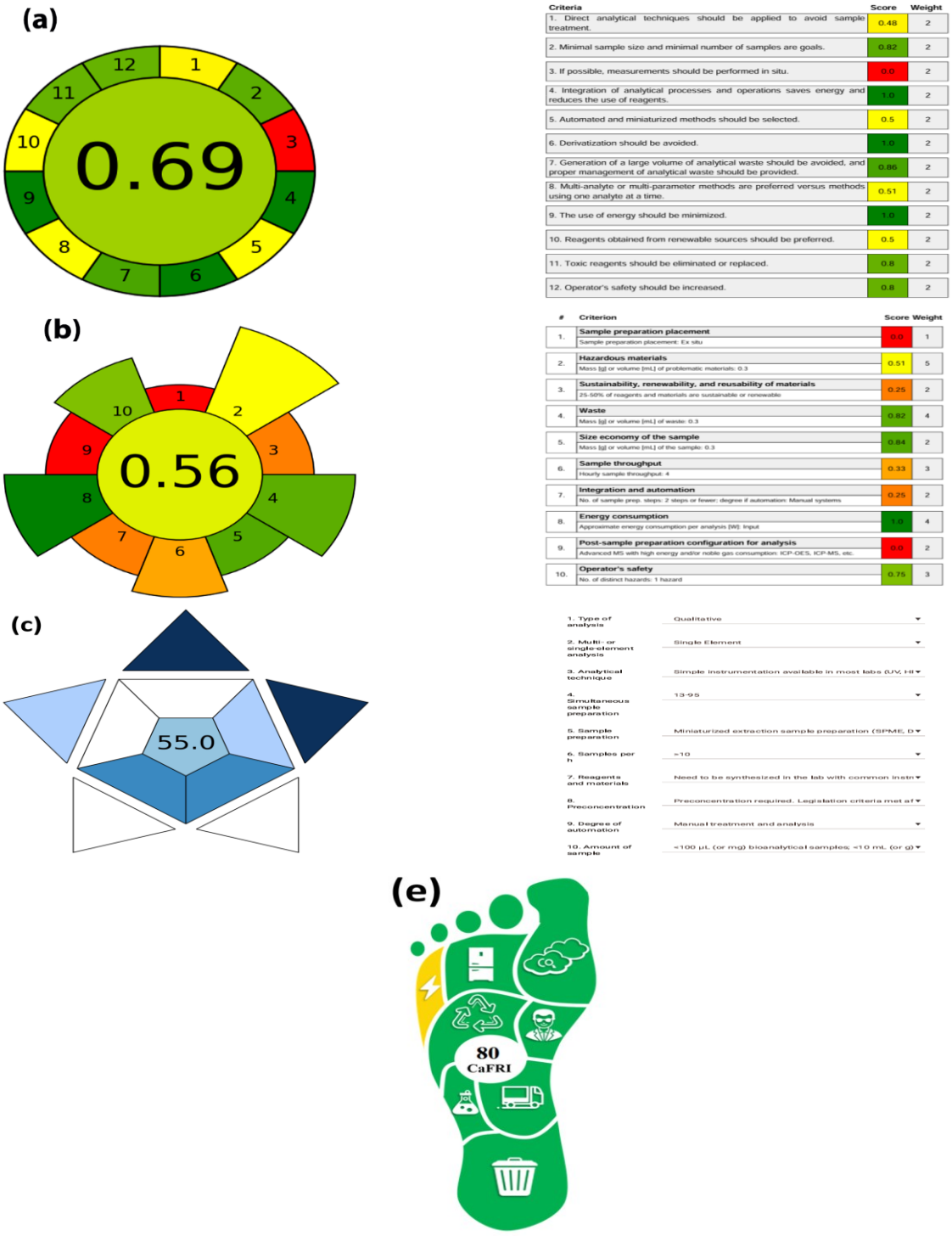

Figure 4. The greenness evaluations of the proposed method: (a) AGREE—Analytical GREEnness Metric Approach, (b) AGREEprep—Analytical greenness metric for sample preparation, (c) the BAGI Index pictogram of the process, and (d) The Carbon Footprint Reduction Index (CaFRI) pictogram

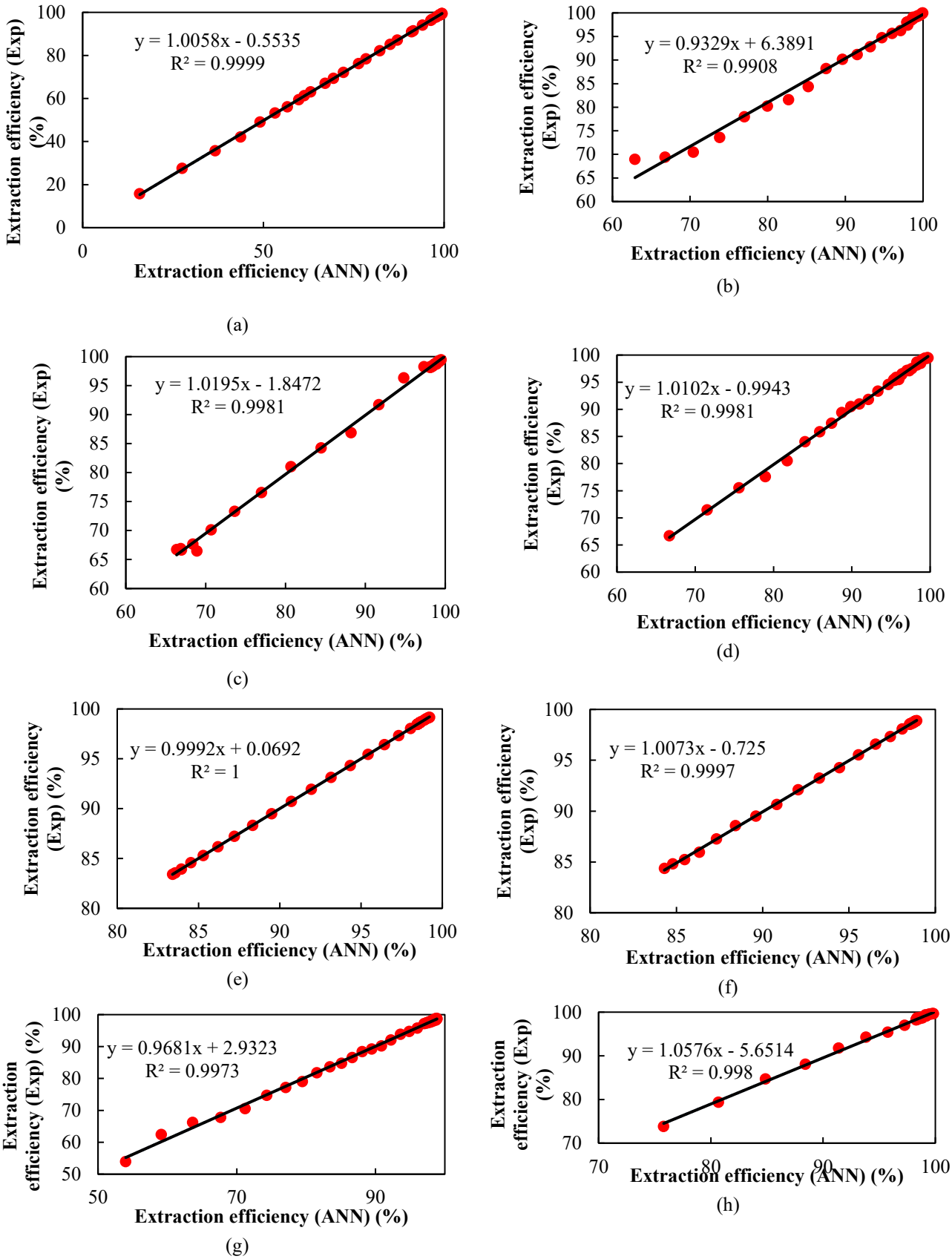

Figure 5. Comparison of experimental (EXP) and predicted results by ANN algorithm for Extraction efficiency for input parameters (a) pH, (b) desorption time, (c) HCl concentration, (d) HCl volume, (e) ionic strength, (r) sample volume, (c) sorbent, and (d) vortex time

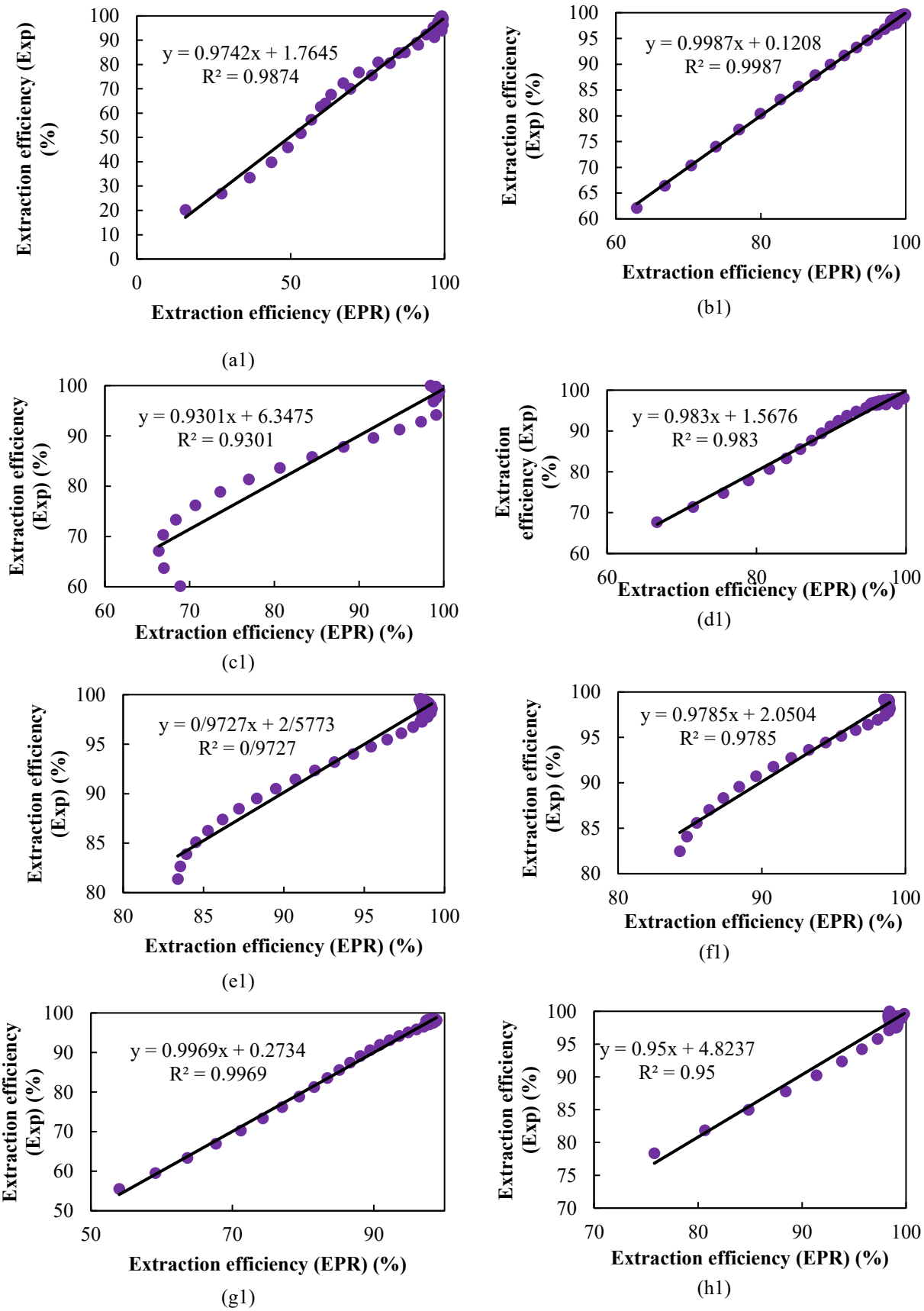

Figure 6. Comparison of experimental (EXP) and predicted results by EPR algorithm for Extraction efficiency for input parameters (a1) pH, (b1) desorption time, (c1) HCl concentration, (d1) HCl volume, (e1) ionic strength, (f1) sample volume, (g1) sorbent, and (h1) vortex time

3.5.1. *Data Results Using EPR*

As can be seen in Fig. 6, the R^2 predicted by EPR for the extraction efficiency ranges from 0.930 to 0.998. In Fig. 6 (b1), $R^2 = 0.9987$ with $y = 0.9987x + 0.1208$, indicating an extremely high correlation for EPR in predicting the extraction efficiency based on the desorption time. The lowest R^2 value is for HCl concentration, with a value of 0.930 and the equation $y = 0.9301x + 6.3475$. In general, the coefficient of determination (R^2) values in all forms indicate that both the ANN and EPR models provide a high degree of correlation between the predicted and experimental extraction efficiencies, with the ANN typically showing slightly higher R^2 values, indicating its superior prediction accuracy. An R^2 value close to 1 indicates that the model predictions closely match the experimental data. In other studies, the EPR algorithm has been used to dry agricultural products and predict the outlet temperature in this process, with R^2 values of 0.910 [53]. In another study, the EPR algorithm was used to predict the outlet air temperature of a solar ventilation device with a phase change material, with an R^2 value of 0.995, which indicates the appropriate accuracy of the above algorithm [52].
The experiments were repeated 3 times, and external validation has already been performed. The ANN and EPR methods were used for the Extraction Efficiency output, which can be seen in Table 2.

Table 2. Validation with external data, with 3 replicates, and prediction by ANN and EPR

PH				Desorption time			
value	Obtained	ANN	EPR	value	Obtained	ANN	EPR
3/5	15/8	15/8	20/21898	30	62/9	68/98409	62/12824
4/5	53/2	53/23757	51/72314	60	89/6	90/18174	89/93073
5/5	72/1	72/19124	76/76975	90	99/3	99/36966	98/79837
6/5	99	99/07621	93/99169	120	98/7	98/86918	99/1529
7/5	99/3	99/36485	99/21677	150	98/0	98/03256	97/99901
8/5	99/1	99/13677	99/90916	30	66/7	69/43938	66/41351
9/5	91	91/00648	88/94894	60	91/5	91/16363	91/71039
10/5	76/3	76/26696	75/61084	90	99/6	99/59503	99/19234
3/5	27/5	27/54648	26/9708	120	98/4	98/42065	98/93469
4/5	56/6	56/11093	57/29281	150	98/2	98/26294	97/92957
5/5	78/4	78/45214	80/88386	30	70/4	70/46757	70/37088
6/5	99/4	99/42056	96/37681	60	93/2	92/81063	93/27353
7/5	98/6	98/70476	99/02184	90	99/8	99/8166	99/4688
8/5	98/7	98/79214	99/49307	120	98/2	98/16484	98/71034
9/5	87	87/08612	85/03828	150	98/7	99/07255	97/92824
10/5	69/4	69/41159	70/07219	HCL volume			
3/5	36/7	35/7894	33/50806	50	66/7	66/70519	67/71786
4/5	59/7	59/48688	62/59325	75	85/8	85/85802	85/58331
5/5	85/1	85/1118	84/67404	100	93/3	93/37079	94/79608
6/5	99/3	99/34778	98/38332	125	99/1	99/24406	97/74392
7/5	98/5	98/58303	99/40454	150	98/3	98/17843	97/86221
8/5	97/8	97/8887	97/59994	200	96/3	96/35574	96/47549
9/5	82/2	82/18063	80/59589	50	71/5	71/483	71/40692
10/5	61/3	61/30002	63/969	75	87/4	87/43544	87/64927
HCL concentration				100	94/6	94/5734	95/67331
0/5	68/9	66/49983	60/13569	125	99/5	99/39312	97/96233
1	77	76/56932	81/35296	150	97/6	97/51907	97/6882
1/5	99/1	99/20823	94/17935	200	97/3	97/13363	96/52729
2	98/4	98/4701	99/99141	50	75/5	75/54856	74/79529

PH			
value	Obtained	ANN	EPR
2/5	98/8	98/9337	100/1657
3	99/3	99/33974	98/26376
0/5	66/9	66/66441	63/73262
1	80/6	81/0303	83/66692
1/5	100/1	100/0628	95/40698
2	98/1	98/33242	100/3294
2/5	99	99/02919	99/81061
3	99/1	99/18839	97/60097
0/5	66/3	66/72934	67/13424
1	84/4	84/2717	85/81365
1/5	100/5	100/4469	96/49549
2	98	98/1997	100/5563
2/5	99/2	99/1617	99/37259
3	98/8	98/78314	96/87128
Ionic strength			
0	98/5	98/49054	97/29612
1	98/5	98/57022	98/98558
2/5	98/5	98/55218	99/56625
5	98/6	98/60139	97/26324
7/5	89/4	89/48954	90/50132
10	83/9	83/94076	83/89884
0	98/6	98/60104	97/82473
1	98/5	98/49371	99/23435
2/5	98/6	98/72566	99/48863
5	98	98/04082	96/71752
7/5	88/3	88/30351	89/5086
10	83/5	83/55964	82/65495
0	98/6	98/6284	98/28181
1	98/4	98/45444	99/41576
2/5	98/8	98/87695	99/34886
5	97/3	97/31582	96/11797
7/5	87/2	87/20611	88/47141
10	83/4	83/39864	81/37284
Sorbent			
5	54	53/9968	55/47072
10	79/4	79/08474	78/8373
15	90/8	90/19436	91/91805
20	98/4	98/09077	97/49033
25	98/1	97/91297	98/39572
30	97/4	97/43275	97/75682
5	59/1	62/48645	59/54381
10	81/5	81/78236	81/27095
15	92/2	92/09067	93/10902
20	98/7	98/34184	97/83538

Desorption time			
value	Obtained	ANN	EPR
75	88/7	89/4435	89/48695
100	95/9	95/52653	96/39464
125	99/7	99/4908	98/08517
150	97	97/15853	97/49103
200	98/8	98/50401	96/66452
Sample volume			
10	98/6	98/59913	98/1922
15	98/8	98/80771	98/80205
20	98/7	98/77415	99/17572
25	98/5	98/52715	99/11945
30	98/8	98/87594	98/43951
35	98	98/07823	96/94212
45	90	90/63086	91/77195
55	85	85/21183	85/60777
10	98/6	98/64693	98/35621
15	98/8	98/84352	98/92517
20	98/6	98/65562	99/20952
25	98/5	98/55164	99/01551
30	98/9	98/88079	98/14936
35	97/3	97/32457	96/41734
45	89/5	89/49548	90/72001
55	84/7	84/81138	84/08846
10	98/7	98/67406	98/51454
15	98/8	98/84971	99/03051
20	98/5	98/57569	99/21344
25	98/6	98/65182	98/86955
30	98/8	98/82525	97/8051
35	96/5	96/5851	95/82634
45	88/4	88/55266	89/58065
55	84/3	84/35217	82/46659
Vortex time			
0/5	75/8	73/8637	78/33431
1	99/1	99/40651	98/13529
1/5	98/6	98/5386	100/2473
2	98/8	98/83917	97/55945
2/5	99/1	99/11691	99/2212
0/5	80/6	79/40771	81/84328
1	99/6	99/591	98/97899
1/5	98/4	98/45861	99/98965
2	98/9	99/05543	97/48917
2/5	98/9	99/01935	100/1148
0/5	84/8	84/73737	84/98153
1	99/8	99/65329	99/61978
1/5	98/3	98/35472	99/67828

PH				Desorption time			
value	Obtained	EPR	ANN	value	Obtained	ANN	EPR
25	97/8	97/65458	98/33149	2	99/1	99/17939	97/53292
30	97/7	97/64685	97/5742	2/5	98/7	98/78504	101/2343
5	63/6	66/23916	63/35841				
10	83/4	83/65398	83/50278				
15	93/5	93/84388	94/15484				
20	98/8	98/68844	98/09197				
25	97/6	97/56768	98/22739				
30	98/2	98/21894	97/39219				

Table 3 presents data from two methods, assessed by RMSE, COV, and R^2. These metrics show that the ANN method excels in predicting extraction efficiency across diverse conditions. Its predictive capabilities are evident despite variations in experimental setups and environmental factors. Notably, the ANN data exhibits less variance than the lab data, indicating more consistent predictions. This stability is illustrated in Scheme 1, highlighting the ANN method's reliability in predicting extraction efficiency. For most parameters (pH, HCl concentration, HCl volume, ionic strength, sample volume, vortex time), ANN shows a higher R^2 than EPR, indicating that ANN generally accounts for a larger proportion of the variance in the experimental data. Notably, for 'Ionic strength', ANN achieves an R^2 of 1, signifying a perfect fit. Lower RMSE values indicate better predictive accuracy. ANN consistently shows significantly lower RMSE values across almost all parameters compared to EPR, suggesting that ANN's predictions are closer to the experimental values. For instance, for 'pH', ANN has an RMSE of 0.325 while EPR has 3.069. Similarly, for 'HCl concentration', ANN's RMSE is 0.595 compared to EPR's 3.244.

Table 3. Statistical data obtained for two artificial neural network methods (ANN and EPR) for the considered parameters

Parameters considered	Algorithm used	R^2	RMSE	COV
PH	ANN	0.999	0.325	0.305
	EPR	0.987	3.069	0.300
Desorption time	ANN	0.990	1.190	0.107
	EPR	0.998	0.378	0.114
HCl concentration	ANN	0.998	0.595	0.140
	EPR	0.930	3.244	0.132
HCl volume	ANN	0.998	0.385	0.092
	EPR	0.983	1.086	0.090
Ionic strength	ANN	1	0.016	0.060
	EPR	0.972	0.923	0.059
Sample volume	ANN	0.999	0.097	0.052
	EPR	0.978	0.715	0.051
sorbent	ANN	0.997	0.759	0.139
	EPR	0.996	0.697	0.143
Vortex time	ANN	0.998	0.425	0.061
	EPR	0.95	1.241	0.056

COV provides a measure of relative variability. Generally, lower COV values are desirable. The COV values for both ANN and EPR are relatively low across all parameters, indicating good precision of both models. The differences in COV between ANN and EPR are less pronounced than for RMSE.

3.5.2. *Limitations or potential overfitting risks of ANN/EPR*

Although high R^2 values were obtained, as shown in Table 3, we emphasize that such values do not automatically rule out overfitting.

To minimize this risk, the following strategies were employed:

•Early stopping based on the validation subset.

•L2 regularization by adjusting the perform Param. regularization parameter.

•Model architecture selection using 5-fold cross-validation.

These steps significantly reduced the likelihood of overfitting, as confirmed by the consistent performance across both validation and test subsets. Nevertheless, we recognize that external validation would further strengthen this conclusion.

Table 4 presents the optimal points (parameters and corresponding extraction efficiency) predicted by the GA coupled with ANN (GA-ANN) and EPR (GA-EPR), and compares them with experimental optimum points. This is crucial for practical applications where optimizing extraction efficiency is the goal. GA-ANN predicts an optimal desorption time of 89.59 with 99.98% efficiency, while GA-EPR suggests 92.76 with 99.72% efficiency. The experimental optimum is 90 for time and 99.3% for efficiency. Both GA-ANN and GA-EPR show good agreement with the experimental values for desorption time and extraction efficiency.

In general, Table 4 indicates that both GA-ANN and GA-EPR algorithms are capable of identifying optimal operating conditions that yield high extraction efficiencies. GA-ANN often provides predictions that are slightly closer to the experimentally determined optimal points for several parameters, particularly for pH, HCl concentration, ionic strength, sample volume, and vortex time. The predicted extraction efficiencies by the GA-optimized models are often very close to or slightly exceed the experimental maximum efficiencies, suggesting the models' potential for process optimization.

Table 4. Comparison of the optimal point with GA for two neural networks (ANN and EPR) with experimental data

Parameters Considered	Optimization With a GA	Optimum Points (prediction)		Optimum Points (Experimental)	
PH	GA-ANN	6.87	101.52	7.5	99
	GA-EPR	7.90	102.43		
Desorption time	GA-ANN	89.59	99.98	90	99.3
	GA-EPR	92.76	99.72		
HCl concentration	GA-ANN	1.32	100.49	1.5	98.5
	GA-EPR	2.31	100.69		
HCl volume	GA-ANN	123.29	99.54	125	99.1
	GA-EPR	126.33	98.12		
Ionic strength	GA-ANN	0	99.15	0	98.5
	GA-EPR	1.43	99.58		
Sample volume	GA-ANN	34.95	98.88	35	98.6
	GA-EPR	29.74	99.21		
sorbent	GA-ANN	19.81	98.85	20	98.1
	GA-EPR	22.25	98.41		
Vortex time	GA-ANN	1	99.69	1	98.8
	GA-EPR	2.5	101.23		

This comprehensive analysis demonstrates the robust predictive capabilities of both ANN and EPR models for optimizing extraction efficiency across various operational parameters. The high R^2 values (consistently above 0.95, and often above 0.99 for ANN) and low RMSE values confirm the accuracy and reliability of these machine learning approaches in predicting experimental outcomes. Specifically, the ANN model generally exhibits superior performance, as indicated by its higher R^2 and lower RMSE values for most parameters. Furthermore, the integration of a GA with these neural networks (GA-ANN and GA-EPR) successfully identifies optimal operating conditions, aligning closely with experimental observations. The predicted optimal extraction efficiencies are remarkably consistent with experimental maximums, validating the utility of these computational models for practical process design and optimization. These findings underscore the significant potential of applying advanced artificial intelligence techniques, particularly ANN coupled with GAs, to precisely model and optimize complex chemical engineering processes like extraction. The detailed statistical data and graphical

correlations presented herein provide strong evidence to support the implementation of these models for enhanced process control and efficiency in relevant industrial or research applications.

3.6. Analytical Performance of the Method

The analytical performance of the method was assessed under the established optimal conditions. This study focuses on the linear range (LR), limit of detection (LOD), limit of quantification (LOQ), relative standard deviation (RSD), and coefficient of determination. The linearity of the samples ranges from 0.2 to 250 µg Kg^{-1} for white rice, wheat flour, and shrimp, and from 0.2 to 200 µg Kg^{-1} for fish. The limits of detection (LODs) were defined as 3Sb/m, where Sb represents the standard deviation of the blank and m denotes the slope of the preconcentration curve. The limits of quantification (LOQs) refer to the lowest measurable concentration level of each target analyte using the proposed method. The limits of detection (LOD) were determined to be 0.052, 0.056, 0.075, and 0.081 µg Kg^{-1}, while the limits of quantification (LOQ) were found to be 0.173, 0.175, 0.186, and 0.269 µg Kg^{-1} for white rice, wheat flour, fish, and shrimp, respectively. The precision of the method was evaluated by determining intra-day and inter-day precision percentages for each sample at three spiked levels, yielding values of less than or equal to 2.8% and 3.3%, respectively. The results are presented in Table 5.

Table 5. The figures of merit of separation and preconcentration of Hg^{2+} via Ag_2O/B@OP-CDs-PT-SPE at optimum conditions

				Precision (%)								
				5 (µg kg^{-1})		25 (µg kg^{-1})		100 (µg kg^{-1})				
Sample	LOD (µg kg^{-1})	LOQ (µg kg^{-1})	LR (µg kg^{-1})	Inter-day (5 days, n=3)	Intra-day (n=6)	Inter-day (5 days, n=3)	Intra-day (n=6)	Inter-day (5 days, n=3)	Intra-day (n=6)	Equation	R^2	EF
White rice	0.052	0.173	0.2-250	3.1	2.5	2.9	2.2	3.1	2.0	Y=16.009X+0.3211	0.9989	274.8
Wheat flour	0.056	0.175	0.2-250	3.3	2.8	3.1	2.4	2.5	2.2	Y=13.334X+0.1824	0.9990	274.2
Fish	0.075	0.186	0.2-200	3.2	2.5	3.3	2.2	2.7	2.3	Y=11.117X+0.6062	0.9989	275.4
Shrimp	0.081	0.269	0.2-250	3.3	2.5	3.2	2.5	2.5	2.1	Y=14.052X+0.8114	0.9989	273.5

1

3.7. Extraction Mechanism

The extraction of Hg^{2+} ions via the Ag_2O/B@OP-CDs nanocomposite is influenced by surface complexation, electrostatic interactions, and redox-assisted adsorption mechanisms. Ag_2O nanoparticles provide numerous surface-active oxygen sites (e.g., –OH, O-) that can establish inner-sphere complexes with mercury ions. In contrast, boron-doped carbon quantum dots (B@CDs) possess functional groups such as –COOH, –OH, and B–O moieties that serve as effective electron-donating and chelating sites. Boron doping alters the electrical structure of the carbon matrix, increasing the affinity for Hg^{2+} through Lewis acid-base interactions. This is consistent with Pearson's HSAB theory, which asserts that Hg^{2+}, as a soft acid, preferentially engages with soft or borderline bases. The Ag^+/Ag^0 redox couple can partially reduce or stabilize Hg^{2+} at the Ag_2O interface, thereby enhancing its retention via redox-assisted adsorption.

At ultra-trace concentrations, the nanocomposite's diverse binding sites, large surface area, and hierarchical structure enable swift and effective mercury extraction. The material demonstrates efficacy in reducing matrix interferences commonly encountered in food analysis, as seen by its notable selectivity and recovery when applied to complex actual matrices, including white rice, wheat flour, fish, and prawns.

This highlights the composite's effectiveness in identifying mercury contamination in agricultural food systems, with significant implications for public health and regulatory compliance (Scheme 3).

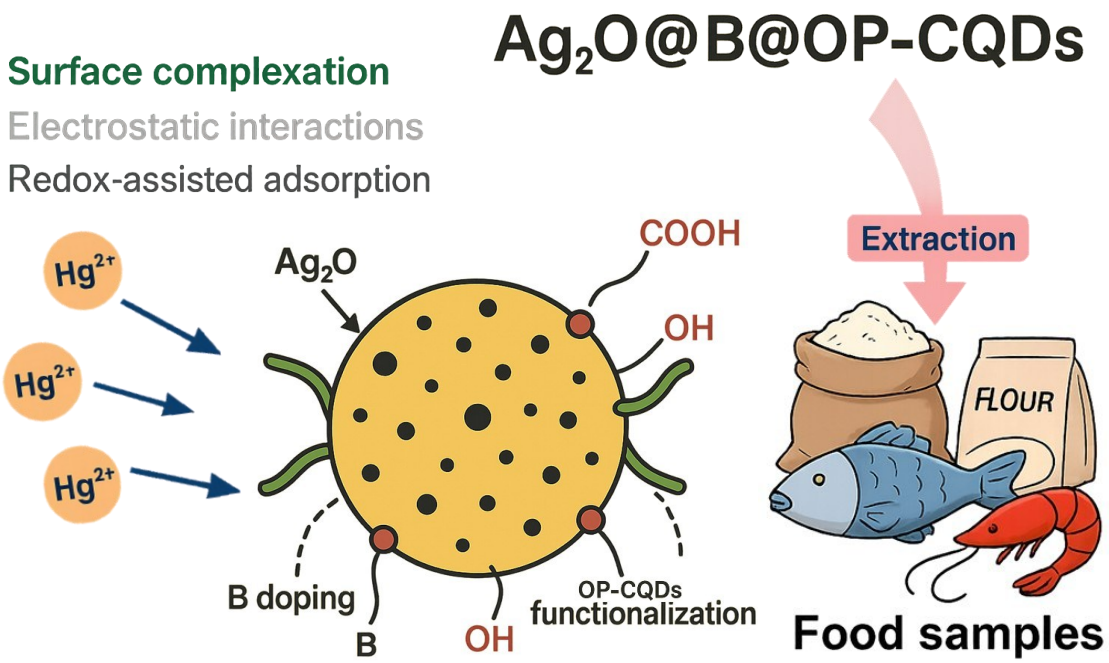

Scheme 3. The Schematic of the extraction mechanism of Hg^{2+} with functional groups of Ag_2O@B@OP-CDs from food samples

3.8. Application of the Method

The utilization of Ag_2O@B@OP-CDs-PT-SPE in conjunction with MP-AES for the preconcentration, separation, and quantification of trace and ultra-trace levels of mercury was examined in samples of white rice, wheat flour, and fish and shrimp. To evaluate the precision of the proposed approach, mercury was introduced into samples of white rice, wheat flour, fish, and shrimp at three concentrations of 5, 25, and 100 µg Kg^{-1}. The relative recoveries (%) ranged from 90.0 to 98.8, with RSDs (%) not exceeding 2.6 (n=3). The findings are presented in Table 6.

Table 6. Ag_2O@B@OP-CDs-PT-SPE coupled with MP-AES for the separation and determination of mercury in food samples

Canned food samples	Spiked concentration (ng Kg^{-1})	Founded (ng Kg^{-1})	Relative recoveries (RR, %)
White rice [a]	-	N. D.[b]	-
	5	4.8 ± 0.3[c]	96.0
	25	24.6 ± 0.5	98.4
	100	98.8± 2.1	98.8
Wheat flour	-	N. D.	-
	5	4.7 ± 0.5	94.0
	25	24.2 ± 0.6	96.8
	100	98.1 ± 2.3	98.1
Fish	-	N. D.	-
	5	4.5 ± 0.3	90.0
	25	23.5 ± 1.5	94.0
	100	94.3 ± 2.7	94.3
Shrimp	-	N. D.	-
	5	4.6 ± 0.6	92.0
	25	24.1 ± 0.5	96.4
	100	96.4 ± 2.5	96.4

[a] White rice and wheat were purchased from a local supermarket in Jiroft, Kerman Province, Iran. Fish and shrimp samples were taken from the Persian Gulf, Bandar Abbas, Hormozgan Province, Iran.
[b] The results are the mean and standard deviation of four replicates (n=3).
[c] N.D. stands for Not Detected.

Table 7. The comparison of Ag_2O@B@OP-CDs-PT-SPE with some recent studies

Analytical method	Adsorbent	Detection method	Sample	LOD [a]	LR [b]	RSD	Reference
PT-SPE	Ag_2O@B@OP-CDs	FI-MP-AES	White rice, wheat flour, fish, and shrimp	0.052-0.081	0.2-250 0.2-200	≤2.8	This study
SPE	Armillae mellea immobilized nanodiamond	ICP-OES	Black tea, water, onion, cheese, and rice	0.13	0.8-33	-	[53]
SPE	Bacillus altitudinis immobilized nanodiamond	ICP-OES	Water, meat, honey, flour, Fruit juice,	0.071	0.625-25	5	[54]
SPE	Geobacillus galactosidasius @Amberlite XAD-4	ICP-OES	Biscuits, flour, rice, Tuna fish, meat, chicken, potato, chocolate, coffee, tap water	0.53	-	8.2	[55]
SPE	Ethylenediamine-modified AC	ICP-OES	Pig liver, water	0.09	-	4	[56]

(a) Limit of detection (LOD) (μg L^{-1}/ μg kg^{-1})
(b) Linear range (LR) (μg L^{-1}/ μg kg^{-1})

3.9. Comparison of the Proposed Method with Other Studies

The efficacy and relevance of the suggested strategy were evaluated against some recently published studies, as summarized in Table 7. Compared with other nanocomposite-based sorbents, including immobilized nanodiamonds and functionalized carbon materials, the Ag_2O/B@OP-CDs–PT-SPE method demonstrates superior analytical performance. Specifically, it provides lower detection limits (0.052–0.081 μg kg^{-1}), a broader linear range (0.2–250 μg kg^{-1}), and higher reproducibility (RSD ≤2.8%) than previously reported systems, which often exhibit narrower linear ranges (e.g., 0.625–25 μg L^{-1}) and higher RSD values.

Importantly, unlike many conventional nanocomposites that rely on synthetic or costly precursors, the current method is derived from agricultural waste (orange peel) and employs a green synthesis pathway, aligning with sustainability principles while achieving excellent enrichment factors.

This unique integration of sustainability and high analytical performance positions Ag_2O/B@OP-CDs as a significant advancement over existing methods for mercury extraction.

4. Conclusion

This study presents the development of a biodegradable Ag_2O/B@OP-CDs nanocomposite, designed as a high-performance sorbent for pipette tip solid phase extraction (PT-SPE) of mercury from intricate food matrices, such as white rice, wheat flour, fish, and prawns. The nanocomposite was synthesised using a green hydrothermal method that included orange peel waste, exemplifying a sustainable utilization of agricultural wastes. This study is the inaugural effort to incorporate Ag_2O and boron into carbon quantum dots derived from orange peel for mercury extraction, while also optimizing the PT-SPE process through sophisticated artificial intelligence models, specifically artificial neural networks (ANN) and evolutionary polynomial regression (EPR), to achieve robust, data-driven parameter optimization. The optimum conditions of 7.5, 20 mg, and 35 mL were obtained for the pH value, amount of sorbent, and sample volume. Moreover, 125 μL of hydrochloric acid with a concentration of 1.5 mol L^{-1} was obtained. The suggested method presents several notable benefits: rapid extraction, reduced consumption of sorbent and solvent, and the total elimination of hazardous organic solvents, aligned with green analytical chemistry principles. The approach exhibited

exceptional analytical performance, characterized by extensive linearity, minimal detection limits, high recovery rates, and remarkable repeatability and reproducibility across various dietary samples. The practical usability and environmental compatibility of the technique were further substantiated by extensive green metrics, including AGREE, AGREEprep, and BAGI, affirming its negligible environmental effect and operational efficiency. This research surpasses traditional mercury extraction techniques by presenting a biodegradable, waste-derived nanocomposite with enhanced binding affinity and illustrating the reliable optimization of the extraction process with artificial intelligence models. The approach demonstrated significant resilience to matrix interferences, with recoveries consistently high despite substantial excesses of coexisting ions, underscoring its robustness for practical food and environmental analysis. Beyond laboratory-scale validation, these outcomes highlight the broader applicability of the method: its greenness, reproducibility, and efficiency make it a promising candidate for adoption in regulatory monitoring of mercury in food, as well as in industrial quality control settings where routine, cost-effective, and environmentally responsible approaches are required.

Declaration of Competing Interest
The authors declare that they have no known competing financial interests or personal relationships that could have appeared to influence the work reported in this paper.

Funding
This study received no funding.

Data availability
Data is available on request. If someone has any questions can contact the corresponding authors.

References

[1] Pang, Y-H., Yang, Q.Y., Jiang, R., Wang, Y.Y., & Shen, X.F. A stack-up electrochemical device based on metal-organic framework modified carbon paper for ultra-trace lead and cadmium ions detection. *Food Chem* 398,133822 (2023)

[2] Parandi, E., Shirani, M., Korrani, Z.S., Teimouri, M., Amirani Poor, M., Sadatfaraji, H., Sarlak, Z., & Shafiei, S. Hybrid inorganic–organic sol–gel @foam for a new development of solid phase extraction of heavy metals. *Emerg Mater* (2025)

[3] Zafar, A., Javed, S., Akram, N., & Naqvi, S.A.R. Health Risks of Mercury. In Kumar N (ed) Mercury Toxicity Mitigation: Sustainable Nexus Approach. Springer Nature Switzerland, Cham, 67-92 (2024)

[4] Fang, S., Zhang, L., Zhao, Y., Zhang, X., Zhang, L., Chen, L., Yoon, J., & Liu, S. Insight into mercury ion detection in environmental samples and imaging in living systems by a near-infrared fluorescent probe. *Sensor Actuator B: Chem* 411,135768 (2024)

[5] Khan, M., & Soylak, M. Deep Eutectic Solvent Based Liquid-Liquid Microextraction of Mercury in Water, Hair and Fish with Spectrophotometric Determination: A Green Protocol. *Anal Lett* 56, 1161-1173 (2023)

[6] Pant, R., Mathpal, N., Chauhan, R., Singh, A., & Gupta, A. A Review of Mercury Contamination in Water and Its Impact on Public Health. In: Kumar N (ed) Mercury Toxicity Mitigation: Sustainable Nexus Approach. Springer Nature Switzerland, Cham, pp 93-115. (2024)

[7] Tuzen, M., Uluozlu, O.D., Karaman, I., & Soylak, M. Mercury(II) and methyl mercury speciation on Streptococcus pyogenes loaded Dowex Optipore SD-2. *J Hazard Mater* 169, 345-350 (2009)

[8] Liu, Y., Chen, L., Su, X., Wang, L., Jiao, Y., Zhou, P., Li, B., Duan, R., & Zhu, G. Constructing an eco-friendly and ratiometric fluorescent sensor for highly efficient detection of mercury ion in environmental samples. *Environ Sci Pollut Research* 31, 4318-4329 (2024)

[9] Sabala, R.F, Zakaria, A.I, Imre, K., Morar, A., Herman, V., & Sallam, K.I. Potential cancer risks associated with the consumption of raw, salted, and canned sardine contaminated by mercury, arsenic, lead, and cadmium in Egypt. *J Food Comp Anal* 134, 106516 (2024)

[10] Abbasi, Y.A, Shahida, S., Ali, A., & Khan, M.H. Liquid–liquid extraction of mercury(II) from aqueous solution using furosemide in benzyl alcohol. *J Radioanal Nuclear Chem* 319, 1029-1036 (2019)

[11] Dogru, S., Yilmaz, E., Gunduz, S.B., & Soylak ,M. An easy and green amine-based microextraction strategy combined UV–Vis spectrophotometric detection for mercury in natural water samples. *J Iran Chem Soci* 18, 3069-3075 (2021)

[12] Ma, S., He, M., Chen, B., Deng, W., Zheng, Q., Hu, B. Magnetic solid phase extraction coupled with inductively coupled plasma mass spectrometry for the speciation of mercury in environmental water and human hair samples. Talanta 146, 93-99 (2016)

[13] Golmohammadpour, M., Ayazi, Z., & Mohammad-Rezaei, R. Electro-assisted solid-phase microextraction of Hg(II) in rice and water samples using NiCo-LDH-MXene fiber. *Food Chem* 470, 142616 (2025)

[14] Nemati, I., Faraji, M., Jafarinejad, S., & Shirani, M. Development of a deep eutectic solvent-based dispersive liquid–liquid microextraction coupled with

spectrophotometer technique for determination of trace amount of Hg(II) in water samples. *Chem Paper* 77, 909-919 (2023)

[15] Ragheb, E., Shamsipur, M., Jalali, F., Sadeghi, M., Babajani, N., & Mafakheri, N. Magnetic solid-phase extraction using metal–organic framework-based biosorbent followed by ligandless deep-eutectic solvent-ultrasounds-assisted dispersive liquid–liquid microextraction (DES-USA-DLLME) for preconcentration of mercury (II). *Microchem J* 166,106209 (2021)

[16] Sun, H., Feng, J., Han, S., Ji, X., Li, C., Feng, J., & Sun, M. Recent advances in micro- and nanomaterial-based adsorbents for pipette-tip solid-phase extraction. *Microchimica Acta* 188, 189 (2021)

[17] Kaykhaii, M., Hashemi, S.H., & Gębicki, J. Applications of metal organic framework adsorbents for pipette-tip micro solid-phase extraction. *TrAC Trend Anal Chem* 179,117877 (2024)

[18] Turoňová, D., Kujovská Krčmová, L., & Švec, F. Application of microextraction in pipette tips in clinical and forensic toxicology. *TrAC Trend Anal Chem* 143, 116404 (2021)

[19] Gidwani, B., Sahu, V., Shukla, S.S., Pandey, R., Joshi, V., Jain, V.K., & Vyas, A. Quantum dots: Prospectives, toxicity, advances and applications. *J Drug Delivery Sci Technol* 61,102308 (2021)

[20] Kambhampati, P. Nanoparticles, Nanocrystals, and Quantum Dots: What are the Implications of Size in Colloidal Nanoscale Materials? *J Phys Chem Lett* 12, 4769-4779 (2021)

[21] de Oliveira BP & da Silva Abreu FOM Carbon quantum dots synthesis from waste and by-products: Perspectives and challenges. *Mater Lett* 282, 128764 (2021)

[22] Doloi, K., Badhai, N., & Mohanta, D. Nanoscale Ag_2O decorated UiO-66 metal organic framework for simultaneous electrochemical sensing of heavy metals, Cd^{2+} and Hg^{2+}. *Mater Research Bullet* 170, 112558 (2024)

[23] Tauanov, Z., Tsakiridis, P.E., Shah, D., & Inglezakis, V.J. Synthetic sodalite doped with silver nanoparticles: Characterization and mercury (II) removal from aqueous solutions. *J Environ Sci Health Part A* 54, 951 (2019)

[24] Wu, Q., Song, J., Wang, Y., Li, H., Zhao, L., Lv, L., & Zhao XE. Carbon quantum dots–functionalized silica stationary phase for pharmaceutical analysis by a green liquid chromatography mode. *Microchim Acta* 189, 175 (2022)

[25] Aladaghlo, Z., Javanbakht, S., Fakhari, A.L., & Shaabani, A. Gelatin microsphere coated Fe_3O_4@graphene quantum dots nanoparticles as a novel magnetic sorbent for ultrasound-assisted dispersive magnetic solid-phase extraction of tricyclic antidepressants in biological samples. *Microchim Acta* 188, 73 (2021)

[26] Rezaei, M. & Ali Mehdinia, A. A Review on the Applications of Quantum Dots in Sample Preparation. *J Sep Sci* (2025)

[27] Wu, Q., Hou, X., Zhang, X., Li, H, Zhao L, & Lv, H. Amphipathic carbon quantum dots-functionalized silica stationary phase for reversed phase/hydrophilic interaction chromatography. *Talanta* 226, 122148 (2021)

[28] Kharangarh, P.R., Ravindra NM, Singh G, & Umapathy S Synthesis of luminescent graphene quantum dots from biomass waste materials for energy-related applications—An overview. *Energ Stor* 5, 390 (2023)

[29] Shirani, M., Parandi, E., Nodeh, H.R., Akbari-adergani, B., & Shahdadi, F. Development of a rapid efficient solid-phase microextraction: An overhead rotating flat surface sorbent based 3-D graphene oxide/ lanthanum nanoparticles @ Ni foam for separation and determination of sulfonamides in animal-based food products. *Food Chem* 373, 131421 (2022

[30] Shirani, M., Salamat, Q., Amirani Poor, M., Nejad, H.M., & Soylak M. Syringe filter-based solid-phase extraction of metronidazole in milk and seafood using cigarette butt-derived activated carbon decorated with $CoMnFe_2O_4$ nanoparticles. *J Food Comp Anal* 142, 107388 (2025)

[31] Xiang, G., Long, S., & Dang, A. Fabrication of the Ordered Mesoporous nZVI/Zr-Ce-SBA-15 Composites Used for Crystal Violet Removal and Their Optimization Using RSM and ANN–PSO. *Sustain* 14, 6566 (2022)

[32] Ismail, U.M., Onaizi, S.A., & Vohra, M.S. Crystal violet removal using ZIF-60: Batch adsorption studies, mechanistic & machine learning modeling. *Environ Technol Innov* 33,103456 (2024

[33] Barghi Jahromi, M.S., Kalantar, V., Akhijahani, H.S., & Salami, P. Application of artificial neural network, evolutionary polynomial regression, and life cycle assessment techniques to predict the performance of a new designed solar air ventilator with phase change material. *Appl Therm Eng* 269, 126117 (2025)

[34] Giustolisi, O., & Savic, D.A. A symbolic data-driven technique based on evolutionary polynomial regression. *J Hydroinform* 8, 207-222 (2006)

[35] Katoch, S., Chauhan, S.S., & Kumar, V. A review on genetic algorithm: past, present, and future. *Multimed Tool Appl* 80, 8091-8126 (2021)

[36] Essekri, A., Laabd, M., & Albourine, A. Efficient adsorption of crystal violet dye using functionalized Argan shell: Experiments and statistical optimization modeling. *Colloid Surf A*: *Physicochem Eng Aspect* 687,133401 (2024)

[37] Manikandan, V., Velmurugan, P., Park, J.H., Chang, W.S., Park, Y.J., Jayanthi, P., Cho, M., & Oh B-T Green synthesis of silver oxide nanoparticles and its antibacterial activity against dental pathogens. *Biotech* 7, 72 (2017)

[38] Mohammad, N.N., Omer, K.M., & Baban, S. Valorization of tire wastes to carbon quantum dots (P-CDs) and photocatalytic degradation enhancement of organic wastes using ZnO-CDs nanocomposites. *J Mater Sci: Mater Electr* 30, 11598-11606 (2019)

[39] John, B.K., Abraham, T., & Mathew, B. A Review on Characterization Techniques for Carbon Quantum Dots

and Their Applications in Agrochemical Residue Detection. *J Fluores* 32, 449-471 (2022)

[40] [40] Wang, T., Xiao, H., Gao, Y., Xu, J., Zhang, Z., Bian, H., & Sun, T. Ag_2O/TiO_2 hollow microsphere heterostructures with exposed high-energy crystal facets and high photocatalytic activities. *J Mater Sci Mater Elect* 31,11496-11507 (2020)

[41] Jin, X., Che, R., Yang, J., Liu, Y., Chen, X., Jiang, Y., Liang, J., Chen, S., & Su, H. Activated Carbon and Carbon Quantum Dots/Titanium Dioxide Composite Based on Waste Rice Noodles: Simultaneous Synthesis and Application in Water Pollution Control. *Nanomater* 12, 472 (2022)

[42] Yavuz, E., Tokalıoğlu, Ş., & Patat, Ş. Magnetic dispersive solid phase extraction with graphene/$ZnFe_2O_4$ nanocomposite adsorbent for the sensitive determination of mercury in water and fish samples by cold vapor atomic absorption spectrometry. *Microchem J* 142, 85-9 3(2018)

[43] Soylak, M., Salamat, Q., & Sajjad, S. Innovative ferrofluid-based vortex-assisted dispersive liquid-liquid microextraction of cadmium and nickel using novel and natural hydrophobic deep eutectic solvent and 2-methylimidazole-coated magnetic nanoparticles. *Microchem J* 211,113050 (2025)

[44] Manousi, N., Płotka-Wasylka, J., & Samanidou, V. Novel sorptive extraction techniques in bioanalysis evaluated by Blue Applicability Grade Index: The paradigm of fabric phase sorptive extraction and capsule phase microextraction. *TrAC Trend Anal Chem* 172,117586 (2024)

[45] Naderi, P., Shirani, M., Semnani, A., & Goli, A. Efficient removal of crystal violet from aqueous solutions with Centaurea stem as a novel biodegradable bioadsorbent using response surface methodology and simulated annealing: Kinetic, isotherm and thermodynamic studies. *Ecotoxicolo Environ Saf* 163, 372-381 (2018)

[46] Dil, E.A., Ghaedi, M., Ghaedi, A., Asfaram, A., Jamshidi, M., & Purkait, M.K. Application of artificial neural network and response surface methodology for the removal of crystal violet by zinc oxide nanorods loaded on activate carbon: kinetics and equilibrium study. *J Taiwan Inst Chem Eng* 59, 210-220 (2016)

[47] Abdel-raoof, A.M., Madbouly, E.A., El-Shanawani, A.A., El-adl, S.M., & Abdelkhalek, A.S. A Lean Six Sigma approach aided improvement for simultaneous electrochemical determination of antiviral drug favipiravir and levodropropizine as an option in the treatment of COVID-19 using glassy carbon electrode modified $NiFe_2O_4$ nanocomposite in different matrices. *Microchem J* 207, 111821 (2024)

[48] Attia, K.A.M., Abdel-Monem, A.H., Abdel-Raoof, A.M., & Eissa, A.S. Simultaneous Determination Of Bisoprolol and Atorvastatin As Single or Co-administrated Drugs in Bulk and Plasma. *Green Asses* 287, 122114 (2023

[49] Kelani, K.M., Gad, A.G., Fayez, Y.M., Mahmoud, A.M., & Abdel-Raoof, A.M. Three developed spectrophotometric methods for determination of a mixture of ofloxacin and ornidazole; application of greenness assessment tools. *BMC Chem* 17,16 (2023)

[50] Atty, S.A., Abdel-raoof, A.M., Fouad, F.A., Mohamed, T.F., & Elbardisy, F.M. Green electrochemical methodology for simultaneous determination of atorvastatin and ezetimibe: Application to biological matrices. *Sust Chem Pharm* 36, 101300 (2023)

[51] Thabet, H.K., Ashmawy, A.F.M., Hosameldin, A.I., & Abdel-Raoof, A.M. Carbon quantum dots biomass waste-derived banana peel as a fluorescence probe for cyclobenzaprine hydrochloride determination in biological fluids and pharmaceuticals aided by green synthesis microwave-driven. *Microchem J* 216, 114700 (2025)

[52] Jahromi, M.S.B., Iranmanesh, M., & Akhijahani, H.S. Thermo-economic analysis of solar drying of Jerusalem artichoke (Helianthus tuberosus L.) integrated with evacuated tube solar collector and phase change material. *J Energ Stor* 52,104688 (2022)

[53] Ozdemir, S., Kılınç, E., Şen, F., Soylak, M. Development of Armillae mellea immobilized nanodiamond for the preconcentrations of Cr(III), Hg(II) and Zn(II). *Anal Biochem* 617, 114122 (2021)

[54] Ozdemir, S., Kilinc, E., Celik, K.S., Okumus, V., & Soylak, M. Simultaneous preconcentrations of Co^{2+}, Cr^{6+}, Hg^{2+} and Pb^{2+} ions by Bacillus altitudinis immobilized nanodiamond prior to their determinations in food samples by ICP-OES. *Food Chem* 215, 447-453(2017)

[55] Kilinc, E., Ozdemir, S., Poli, A., Niolaus, B., Romano, I., Bekmezci, M., & Sen, F. A novel bio-solid phase extractor for preconcentrations of Hg and Sn in food samples. *Environ Research* 207,112231 (2022)

[56] Li, Z., Chang, X., Zou, X., Zhu, X., Nie, R., Hu, Z., & Li, R. Chemically-modified activated carbon with ethylenediamine for selective solid-phase extraction and preconcentration of metal ions. *Anal Chim Acta* 632, 272-277 (2009)

2008-9244 [https://doi.org/10.57647/jnsc.2025.1506.26]